Study on the dust layer development caused by a cold frontal system using the lidar network in the Gobi Desert

（ゴビ砂漠のライダーネットワークを用いた
寒冷前線システムによるダスト層の発達に関する研究）

KAWAI, Kei

（河合　慶）

A dissertation for the degree of Doctor of Science

Department of Earth and Environmental Sciences,

Graduate School of Environmental Studies, Nagoya University

（名古屋大学大学院環境学研究科地球環境科学専攻学位論文　博士（理学））

2018

Abstract

Asian dust (Kosa in Japanese) affects the climate system and human activity through the radiative balance and atmospheric quality. The dust is emitted from the ground surface by strong wind in arid and semi-arid regions of East Asia. If the emitted dust can reach from the atmospheric boundary layer to the free troposphere above, it is transported over a long range to the North Pacific region by the middle-latitude westerlies. Thus, the spatial distribution of dust in the source regions is a key factor in the subsequent long-range transport of the dust. In the Gobi Desert, which is one of the major source regions of Asian dust, almost all dust events arise from cold frontal activity. Therefore, it is necessary to reveal dust outbreak caused by a cold frontal system and the spatial distribution of the dust.

In the eastern part of the Gobi Desert (Sainshand and Zamyn-Uud, Mongolia), lidar observations are operated by the National Institute for Environmental Studies, Japan. In the present study, a ceilometer (compact lidar) observation is conducted in the central part of the Gobi Desert (Dalanzadgad, Mongolia). The automated observation system for the ceilometer was developed. This study used these three lidars as a network to show the spatial distribution of dust in the Gobi Desert. In this study, a dust event on 22–23 May 2013, which was caused by a cold frontal system, was analyzed by using the lidar network as well as various meteorological data (e.g., SYNOP surface meteorological observation data, NCEP-FNL objective analysis data, and trajectory analyses using the HYSPLIT model). The objective of this study is to show the spatial development of a dust layer by a cold frontal system and the subsequent long-range transport of the dust.

During this dust event, the cold front of an extratropical cyclone crossed the Gobi Desert southeastward and sequentially passed through Dalanzadgad, Sainshand, and Zamyn-Uud. The cold air behind the cold front advected southeastward, and the warm air in front of the cold

front was ascended around the cold front. In Dalanzadgad, located in the central part of the Gobi Desert, a dust storm occurred owing to the strong wind (6–10 m/s) associated with the cold front. A part of the dust ascended along the cold frontal surface and reached a height of 1.6 km above ground level. The dust was transported by the ascending warm air in the cold frontal system. After that, the dust moved to the eastern part of the Gobi Desert together with the cold frontal system. In Sainshand and Zamyn-Uud, located in the eastern part of the Gobi Desert, the dust layer along the cold frontal surface extended from the atmospheric boundary layer to the free troposphere. The spatial development of the dust layer was caused by the updraft of the warm air in the cold frontal system.

In conclusion, based on the lidar network observation and the various meteorological data, this study showed that a cold frontal system developed a dust layer from the atmospheric boundary layer to the free troposphere while moving over the Gobi Desert. The mechanism of this development can be explained by two processes as follows: (1) the continuous emission of dust from the desert surface to the atmospheric boundary layer by the strong wind associated with the cold front and (2) the continuous transport of the dust from the atmospheric boundary layer to the free troposphere by the updraft of the warm air in the cold frontal system. This mechanism can lead to the long-range transport of dust by the westerlies in the free troposphere. It is the primary outcome of this study to capture the mass transport of a cold frontal system.

This study focused on the cold frontal activity which frequently induces dust outbreaks in the Gobi Desert, and showed the spatial structure of the generation and development of a dust layer caused by a cold frontal system. This outcome can contribute to the elucidation of the long-range transport of Asian dust and an improvement in the accuracy of climate models.

論文要旨

　アジアダスト（黄砂）は、放射収支や大気環境を通して、気候システムや人間活動に影響を与える。東アジアの乾燥・半乾燥地域において、強風によって地表面から舞い上げられたダストは、大気境界層から上空の自由対流圏に到達すると、偏西風によって北太平洋地域へ長距離輸送される。このように、発生源におけるダストの空間分布はその後の長距離輸送に大きく関わっている。アジアダストの主要な発生源の一つであるゴビ砂漠では、ダストイベントのほとんどが寒冷前線活動によって引き起こされている。したがって、寒冷前線システムによるダストの舞い上げとその空間分布を明らかにする必要がある。

　ゴビ砂漠の東部（モンゴルのサインシャンドとザミンウド）には、日本の国立環境研究所のライダーが設置されている。本研究では、ゴビ砂漠の中央部（モンゴルのダランザドガド）にシーロメーター（簡易型ライダー）を設置し、自動観測システムを構築した。ゴビ砂漠におけるダストの空間分布を捉えるために、これら3地点のライダーをネットワークとして利用した。このライダーネットワークと様々な気象データ（SYNOP 地上気象観測データ、NCEP-FNL 客観解析データ、HYSPLIT モデルの流跡線解析など）を用いて、寒冷前線の通過に伴って発生した、2013 年 5 月 22〜23 日のダストイベントを解析した。本研究の目的は、寒冷前線システムによるダスト層の空間的な発達とその後の長距離輸送を明らかにすることである。

　このダストイベントの間、温帯低気圧に伴う寒冷前線がゴビ砂漠を南東方向に横断し、ダランザドガド、サインシャンド、ザミンウドの順に通過した。寒冷前線後面の寒気は南東方向に移流し、寒冷前線前面の暖気は寒冷前線付近で持ち上げられた。ゴビ砂漠中央部のダランザドガドでは、寒冷前線に伴う強風（6〜10 m/s）によってダストストームが発生した。一部のダストは寒冷前線面に沿って地上から高度 1.6 km まで上昇した。このダストは寒冷前線システム内の暖気の上昇流によって輸送された。

その後、寒冷前線システムとともにゴビ砂漠の東部へ移動した。ゴビ砂漠東部のサインシャンドとザミンウドでは、寒冷前線面に沿って分布するダスト層は、大気境界層から自由対流圏まで広がっていた。このダスト層の拡大は、寒冷前線システムにおける暖気の上昇流によってもたらされた。

　以上から、ライダーネットワークの観測結果と各種の気象データを組み合わせて解析することにより、寒冷前線システムがゴビ砂漠を移動する間に、ダスト層を大気境界層から自由対流圏まで発達させる様子が明らかになった。この発達のメカニズムは以下の 2 つのプロセスによって説明できる：（1）寒冷前線に伴う強風による砂漠地表面から大気境界層へのダストの継続的な供給、（2）寒冷前線システムにおける暖気の上昇流による大気境界層から自由対流圏へのダストの継続的な輸送。このメカニズムは自由対流圏の偏西風によるダストの長距離輸送をもたらす。寒冷前線システムによって実際に物質輸送が行われた様子を捉えたことは、本研究の主要な成果である。

　本研究では、ゴビ砂漠のダスト発生の主要因である寒冷前線活動に着目し、寒冷前線システムによるダスト層の発生と発達の空間構造を明らかにした。これにより、アジアダストの長距離輸送の解明や気候モデルの精度向上に貢献することができる。

Contents

1. Introduction

1.1 Overview and Outbreak of Asian dust

Asian dust, called Kosa in Japan, is generated in arid and semi-arid regions of East Asia (e.g., Kurosaki and Mikami, 2005) and transported over a long range to the North Pacific region (e.g., Husar et al. 2001). The dust affects the climate system both directly and indirectly (Huang et al., 2014). Also, the dust influences human activity and health not only in the source regions but also in the downwind regions (Jugder et al., 2011; Kwon et al., 2002; Higashi et al., 2014).

Asian dust is emitted from the ground surface to the atmosphere in arid and semi-arid regions of East Asia by strong wind. The main source regions of the Asian dust are the Gobi Desert, the Taklimakan Desert, and the Loess Plateau (Fig. 1.1a) (e.g., Kurosaki and Mikami, 2005). The Gobi Desert extends from southern Mongolia to western Inner Mongolia, China. The Taklimakan Desert spreads in the Tarim Basin in western China, which is surrounded by the Tianshan Mountains on the north, the Pamir Plateau on the west, and the Kunlun Mountains on the south. The Loess Plateau is located around the middle basin of the Yellow River in central China. The vegetation indexes in these source regions were low (<0.3) in May 2013 (Fig. 1.1b). These regions play an important role in the emission of the Asian dust.

The frequency of dust occurrence in the source regions has been studied by using dust observation data from meteorological stations, such as the present weather of the SYNOP report (World Meteorological Organization, 1995). Sun et al. (2001) analyzed dust storm reports from meteorological stations in China and Mongolia during 1960–1999 and showed that the Gobi Desert and the Taklimakan Desert were dominant source regions of Asian dust. Natsagdorj et al. (2003) investigated the number of days with dust storms in Mongolia between 1937 and 1999 and concluded that the Gobi Desert was a source area for the formation of dust storm. Kurosaki and Mikami (2005) analyzed surface meteorological data in East Asia during 1988–2004 and reported that dust outbreaks frequently occurred in the Gobi Desert, the western part

of the Loess Plateau, and the Taklimakan Desert. Wu et al. (2016) revealed that the highest dust outbreak frequency in East Asia was recorded in the Gobi Desert in 1999–2013. In summary, the three major source regions of Asian dust have affected the emission of the dust from the past to the present.

The frequency of dust occurrence in the source regions has a seasonal variation. Kurosaki and Mikami (2005) showed that dust outbreak frequency in the source regions varies seasonally and reached its maximum in spring. They also found that the secondary weaker peaks occurred in autumn except in the Taklimakan Desert, and that dust outbreaks frequently occurred only in the Taklimakan Desert even in summer. Natsagdorj et al. (2003) reported that the highest frequency of dust storms occurs in spring (61%), and a second maximum frequency occurs in autumn (22%) in Mongolia between 1960 and 1999. Sun et al. (2001) showed that the monthly percentages of dust storm occurrence in China and Mongolia in the spring of 1960–1999 were 20% in March, 58% in April, and 22% in May.

The frequency of dust occurrence in the source regions has an inter-annual variation (Fig. 1.2). Natsagdorj et al. (2003) revealed that the number of dusty days during the period of 1960–1999 increased three-fold from 15 days in 1960s to 50 days in 1980s and decreased to 40 days in 1990s (Fig. 1.2a). Sun et al. (2001) found that the highest rate of dust storms in China occurred in the 1970s (21 in total) during the period of 1960–1999 (Fig. 1.2b). Wu and Kai (2016) reported that the occurrence of dust outbreaks in the Gobi Desert and northern China during the period of 1999–2013 was highest between 2000 and 2002 (9–12% days in each year), followed by 2006 (10%), and then decreased significantly between 2007 and 2013 (3%) (Fig. 1.2c).
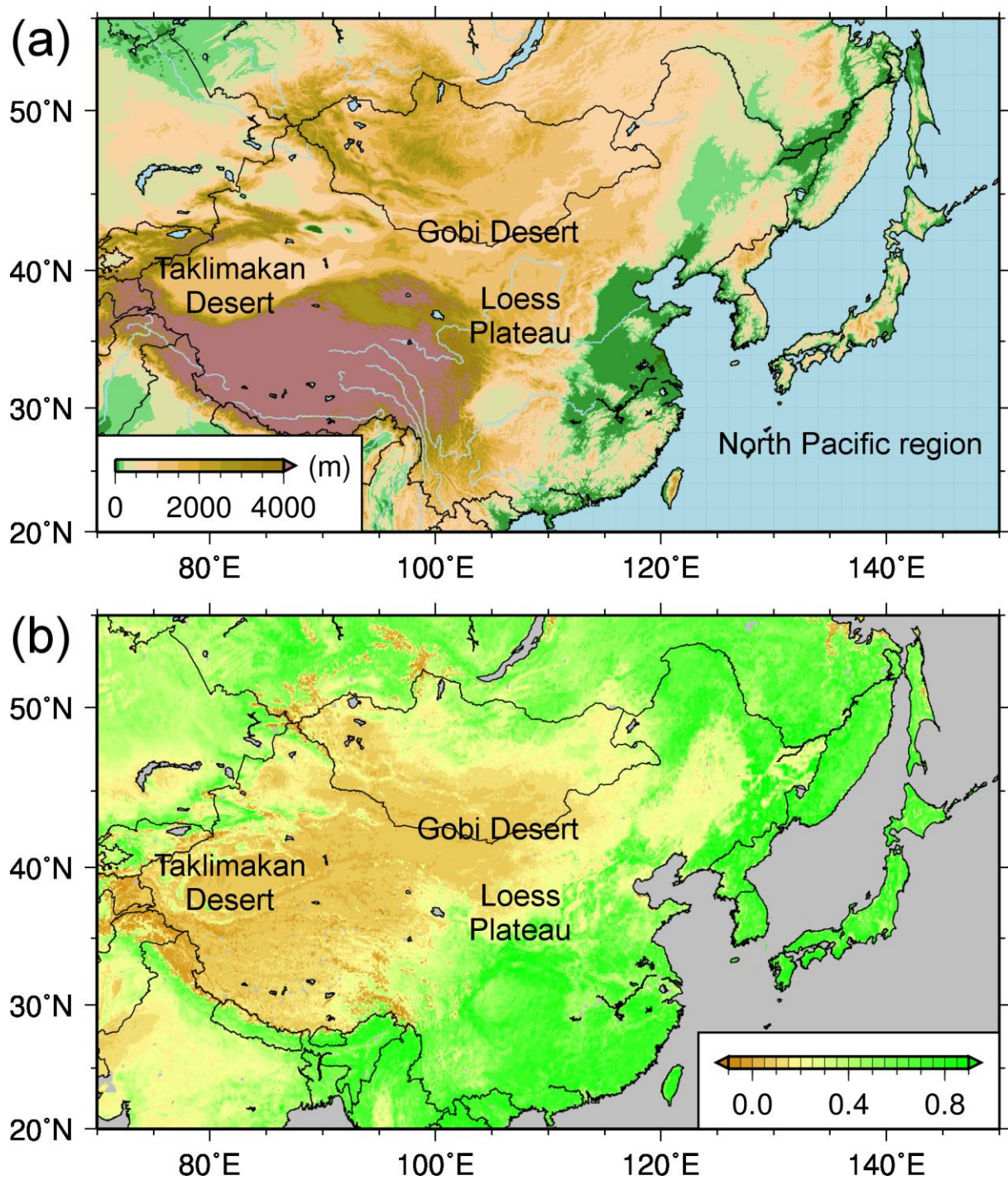
Figure 1.1: (a) Topography and (b) vegetation index in East Asia. (a) The color scale of altitude is shown in the lower-left legend. (b) The vegetation index is the monthly-averaged NDVI (Normalized Difference Vegetation Index) in May 2013 derived from the MODIS onboard the Terra satellite.
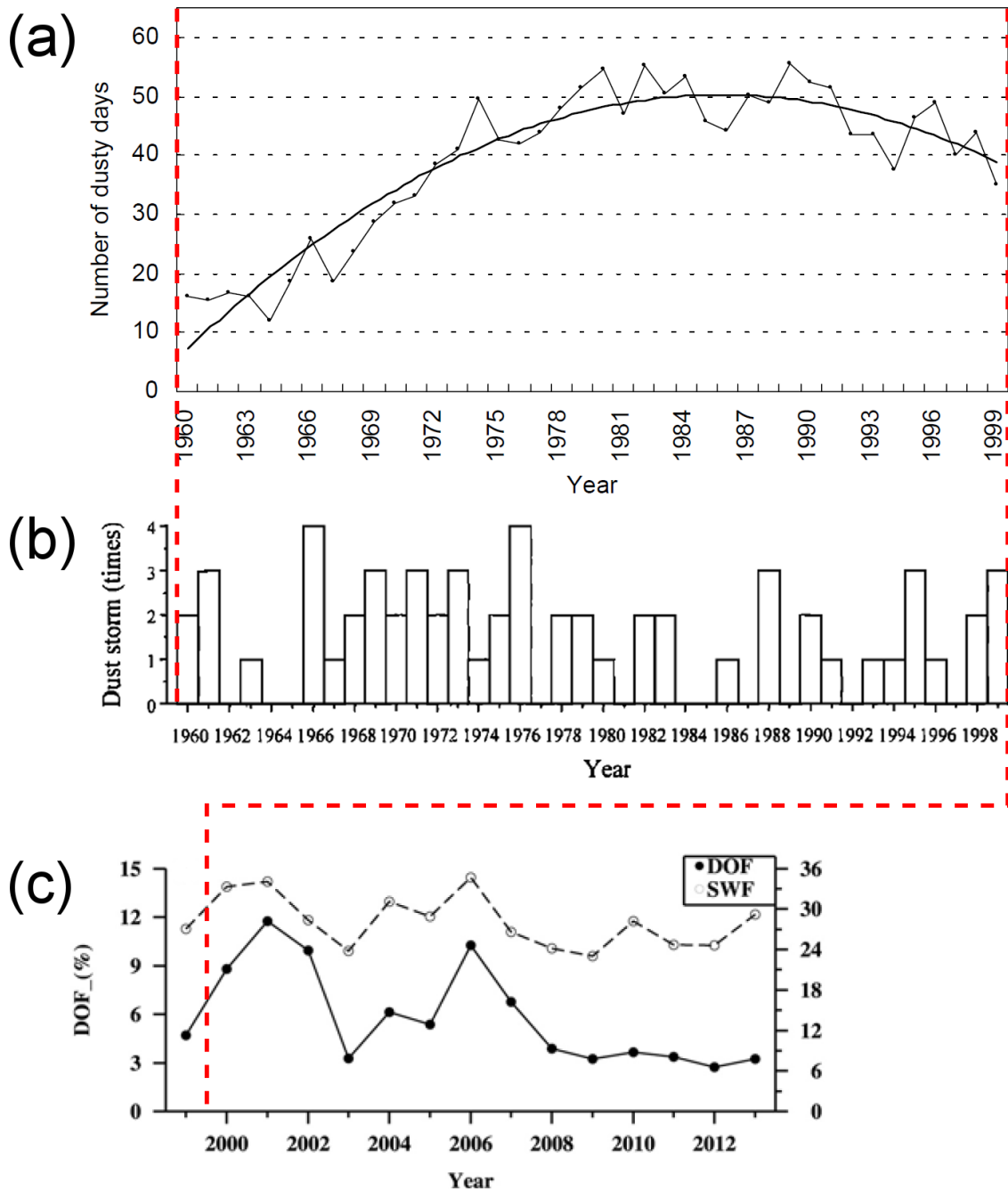
Figure 1.2: Time series of (a) the number of dusty days in Mongolia and its trend (thick line) from 1960 to 1999 (Natsagdorj et al., 2003), (b) the number of dust storms in arid and semi-arid regions of China from 1960 to 1999 (Sun et al., 2001), and (c) the frequencies of dust outbreak (DOF) and strong wind (SWF) in the Gobi Desert and northern China from 1999 to 2013 (Wu and Kai, 2016). Each of the red broken lines indicates the same time in the panels.

1.2 Long-range transport of Asian dust

Asian dust has been observed in the North Pacific region such as Korea, Japan, and the Pacific Islands. For example, the Asian dust (Kosa) was observed in Japan mainly in spring every year (Fig. 1.3). The number of dusty days in Japan had a peak in 2000–2002, which is consistent with frequent dust outbreaks in the Gobi Desert and northern China (Wu and Kai, 2016) (Fig. 1.2c).

Duce et al. (1980) analyzed the Al component of atmospheric particulate matter collected in the Marshall Islands from April to August 1979, and suggested that soil dust came from Asia with anticyclonic circulation in May 1979 in consideration of backward trajectory analysis. Shaw (1980) reported that Asian dust reached Hawaii in April to May 1979 by using a sunphotometer observation in Hawaii and backward trajectory analysis. Iwasaka et al. (1983) showed the transport and spatial scale of dust in April 1979 by analyzing a lidar observation data in Nagoya, geostationary meteorological satellite images, and backward trajectories. The lidar observed two distinct dust layers at heights of 2 and 6 km, which were probably transported from the Gobi Desert and the Taklimakan Desert, respectively.

Kai et al. (1988) observed dust layers at a height of 2–4 km by lidar in Tsukuba, Japan, and showed that the dust was transported from the Loess Plateau and the Taklimakan Desert by the westerlies, based on numerical simulations. Husar et al. (2001) analyzed two intense dust storms in the Gobi Desert on 15 and 19 April 1998 and the following long-range transport by using various remote sensing and in-situ measurements. They reported that the dust cloud generated from the second dust storm crossed the Pacific Ocean in 5 days and reached the mainland of USA. Hara et al. (2009) showed the three-dimensional structures of dust transport from the Gobi Desert and the Loess Plateau through the atmospheric boundary layer and the free atmosphere during the end of May 2007 by using a space-borne lidar (the Cloud-Aerosol Lidar with Orthogonal Polarization; CALIOP) and a dust transport model with data assimilation

based on a ground-based lidar network in East Asia. Yumimoto et al. (2009) reported that an optically thin, highly elevated, horizontally extensive dust veil was transported from the Taklimakan Desert to eastern Asia, the Pacific Ocean, North America, and the Atlantic Ocean, based on the space-borne lidar CALIOP and a three-dimensional global aerosol transport model (SPRINTARS). Uno et al. (2009) demonstrated that the dust generated from an extensive dust storm in the Taklimakan Desert on 8–9 May 2007 was transported more than one full circuit around the globe in about 13 days by using the space-borne lidar CALIOP and the SPRINTARS model.

In summary, the long-range transport of Asian dust is caused by the following mechanism (Fig. 1.4). In the source regions, dust is emitted from the ground surface to the atmospheric boundary layer (ABL) by strong wind. If the emitted dust can reach from the ABL to the free troposphere above, it is transported over a long range to the North Pacific region by the middle-latitude westerlies. The dust remaining in the ABL over the source region is deposited around. Therefore, the spatial distribution of dust in the source regions is a key factor in the long-range transport of dust.
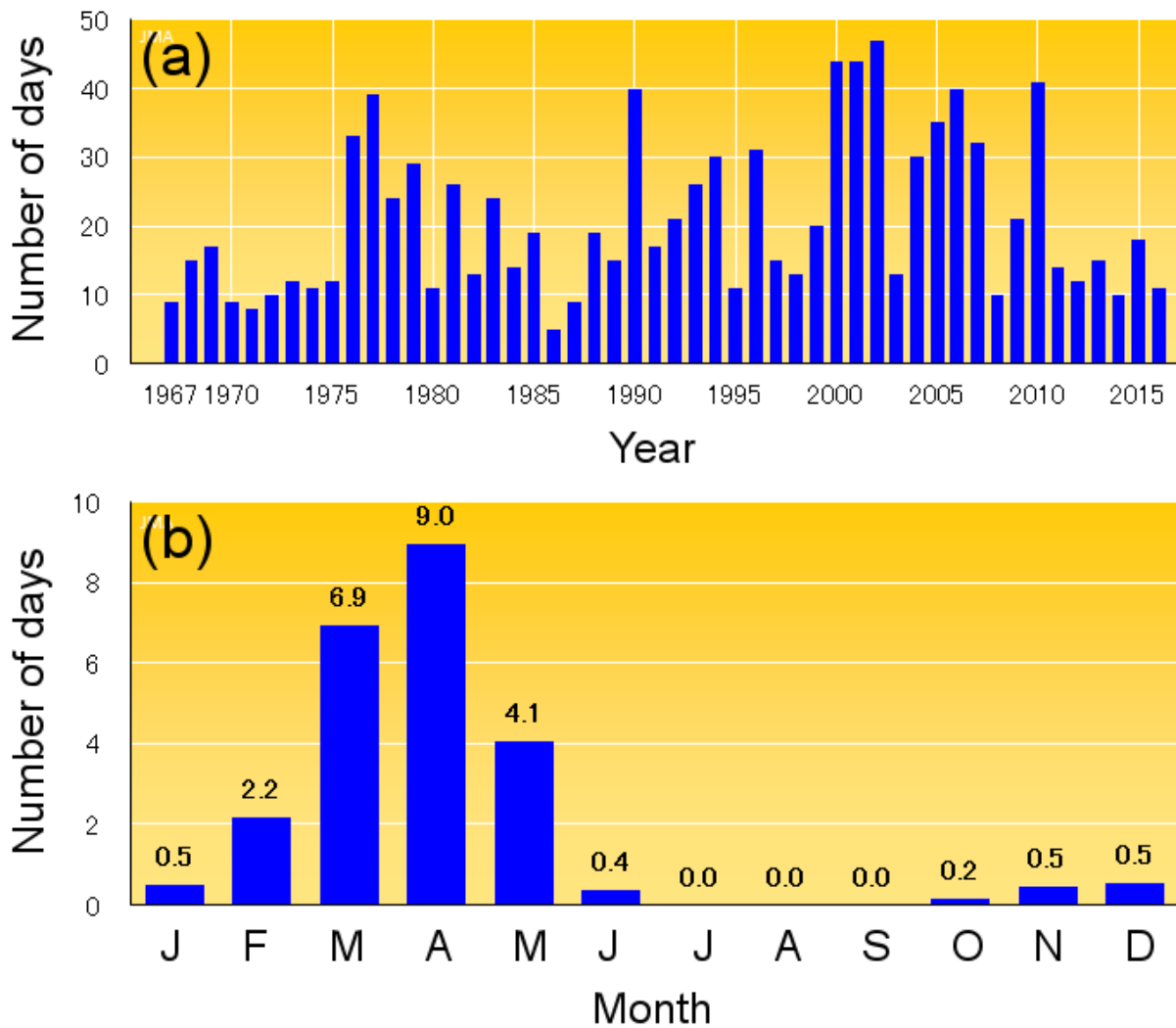
Figure 1.3: Number of days on which Asian dust was observed in Japan (partly modified from http://www.data.jma.go.jp/gmd/env/kosahp/kosa_shindan.html). (a) Annual total number of the days from 1967 to 2016 and (b) monthly-averaged number of the days between 1981 and 2010. The number of the meteorological stations for the Asian dust observation used in these analyses was 59.
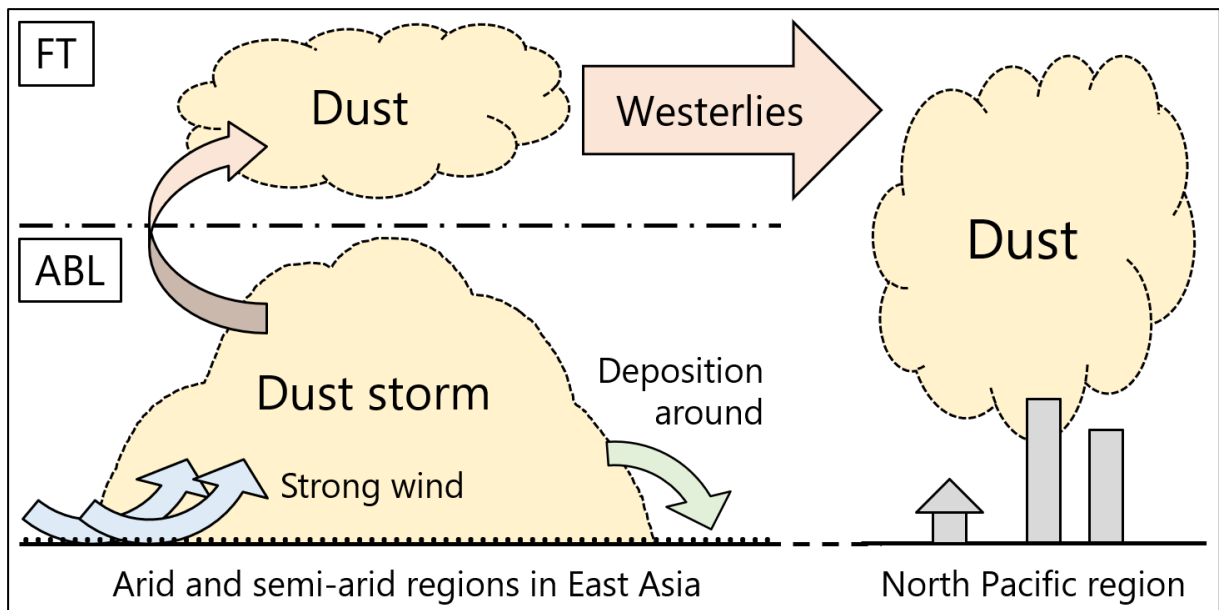
Figure 1.4: Mechanism of the long-range transport of Asian dust shown by previous studies (e.g., Kai et al., 1988; Husar et al., 2001). In the arid and semi-arid regions of East Asia, dust is emitted from the ground surface to the atmospheric boundary layer (ABL) by strong wind. If the dust can reach the free troposphere (FT), it is transported over a long range to the North Pacific region by the middle-latitude westerlies. The dust remaining in the ABL over the source region is deposited around.

1.3 Analysis target and objectives of this thesis

Ground-based lidars are effective for observing vertical distribution of dust continuously. Although it is necessary to install lidars in the source regions of Asian dust, their severe environment makes it difficult. Nevertheless, some lidars are operated in the source regions beyond the difficulties. In the Taklimakan Desert, a depolarization lidar was installed in 2002 through the Japan–China Joint Studies on Origin and Transport of Aeolian Dust and its Impact on Climate (ADEC) (Tsunematsu et al., 2005; Kai et al., 2008). In the Loess Plateau, a group from Lanzhou University, China, conducts a lidar observation with many other measurements (Huang et al., 2008). In the Gobi Desert, the National Institute for Environmental Studies (NIES), Japan, operates two lidar observations from 2007 in Sainshand and Zamyn-Uud, Mongolia (the yellow-filled circles in Fig. 1.5) (Sugimoto et al., 2008). Also, Kai Laboratory of Nagoya University, including the author, conducts two ceilometer (compact lidar) observations from 2013 and 2017 in Dalanzadgad and Mandalgobi, Mongolia, respectively (the red-filled circles in Fig. 1.5) (Kawai et al., 2015).

In the Gobi Desert, almost all dust events arise from cold frontal activity (Shao and Wang, 2003; Takemi and Seino, 2005). A cold front often passes through the desert in spring (Hayasaki et al., 2006). This must be related to frequent cyclogenesis in the lee of the Altai-Hangayn-Sayan Mountains (Fig. 1.5) in spring (Chen et al., 1991; Adachi and Kimura, 2007; Wang et al., 2009). Therefore, it is important to understand the relationship between dust events and cold fronts. In previous studies, dust events associated with cold fronts were analyzed via satellite images and numerical models (Husar et al., 2001; Adachi et al., 2007; Hara et al., 2009). However, the spatial relationship between dust events and cold fronts, which involves the long-range transport of dust, is not well known because of the lack of lidar observation results in the source region of dust.

A dust event occurred in the Gobi Desert during the passage of a cold front on 22–23

May 2013. Our previous study showed dust transport from the ABL to the free troposphere by the cold frontal system during the dust event, based on the lidar in the central part of the desert (Kawai et al., 2015). In the present study, we combined the three lidars in the desert into a lidar network (Kawai et al., 2018). The purpose of the present study is to show the spatial development of a dust layer and the long-range transport of the dust during the dust event by using the lidar network.

This thesis is organized in the following way. In this section (Section 1), the outbreak and long-range transport of Asian dust as well as the analysis target and objectives of this thesis were introduced. Section 2 describes the three lidar observations in the Gobi Desert and meteorological data used in this study. Meteorological conditions in Mongolia and observations and analyses results in the three lidar observation sites are presented in Section 3. In Section 4, the upward transport of dust by the cold frontal system, the dust layer development caused by the cold frontal system, and the long-range transport of the dust are discussed. Finally, Section 5 summarizes the conclusion of this study.
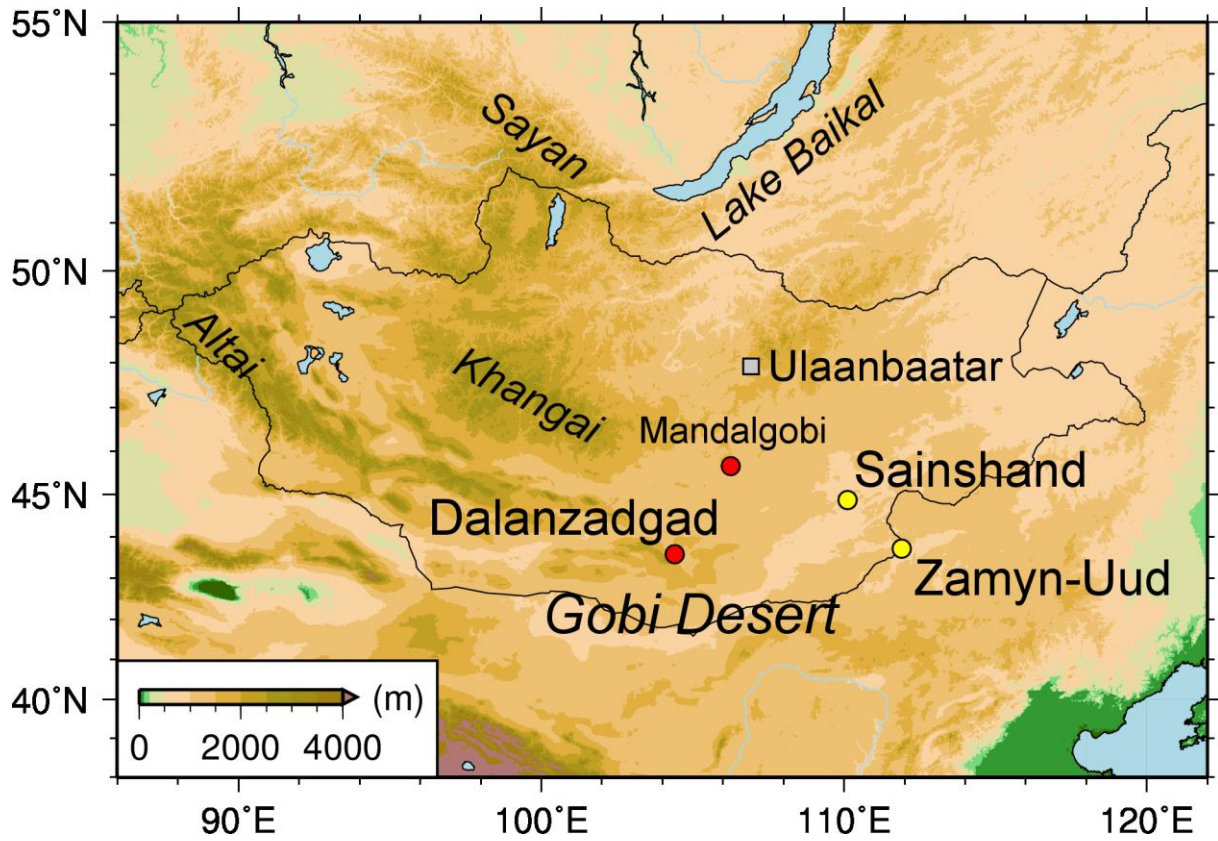
Figure 1.5: Topographic map of Mongolia and its surrounding region. The color scale of altitude is shown in the lower-left legend. The circles filled with red and yellow indicate the ceilometer observation sites and the NIES lidar observation sites in the Gobi Desert, respectively.

2. Observations and data

2.1 Ceilometer observation in Dalanzadgad, Mongolia

A ceilometer observation has been conducted in Dalanzadgad in southern Mongolia since 29 April 2013 (Fig. 1.5). The ceilometer observation is a part of the collaborative research between Graduate School of Environmental Studies, Nagoya University, Japan, and the Information and Research Institute of Meteorology, Hydrology and Environment (IRIMHE), Mongolia. I am in charge of the installation, monitoring, maintenance, and data management of the ceilometer observation. For the installation and maintenance, I have visited Dalanzadgad seven times between April 2013 and May 2017 (in April–May 2013, September 2013, April–May 2014, March 2015, April–May 2015, April–May 2016, and April–May 2017).

2.1.1 Observation site

The ceilometer observation site is the Dalanzadgad Meteorological Observatory (43.58°N, 104.42°E, 1470 m above sea level (ASL)), which is situated in the town of Dalanzadgad (Fig. 2.1). The ceilometer used was installed in front of the main building of the observatory (Fig. 2.2). Dalanzadgad is located in the central part of the Gobi Desert and to the southeast of the Altai and Khangai Mountains (Fig. 1.5). The distance from Ulaanbaatar, the capital of Mongolia, is about 520 km in a straight line.

2.1.2 Observation instrument

The ceilometer used in this observation is Vaisala CL51, which is a compact backscatter lidar that is easy to operate and maintain. The laser wavelength of the ceilometer is 910 nm, the pulse repetition rate is 6.5 kHz, and the pulse energy is 3.0 μJ. The ceilometer has a window blower to remove light contamination on the observation window automatically. The internal battery of the ceilometer enables the observation for about two hours during a power cut. The

power and data cables run through pipes from the ceilometer into the main building of the observatory (Fig. 2.2).

2.1.3 Observation system

The automated observation system of the ceilometer was developed and is illustrated in Fig. 2.3. It consists of four sub-systems for data collection, transfer, analysis, and distribution. The ceilometer is connected to a laptop computer installed in the main building of the observatory through a data cable. First, the ceilometer sends observation data to the computer every 6 sec. Then, the computer stores the observation data in a data file every hour. Finally, the data file is transferred to a server in Prof. Kai's Laboratory of Nagoya University through the Internet every hour.

The server makes a figure of the observation data for latest 24 hours and uploads it on the web site of the ceilometer observation every hour automatically (Fig. 2.4). I monitor the condition of the ceilometer observation through the figure every day. If the ceilometer observation stops, I check the laptop computer in Dalanzadgad through the Internet.

2.1.4 Observation data

The ceilometer measures the intensity P(z) of backscatter light of emitted laser pulses from scatterers in the atmosphere. The signal power P(z) received from height z by a lidar including a ceilometer is derived from the lidar equation as follows:

$$P(z) = K \, O(z) \, \frac{\beta(z)}{z^2} \, \exp(-2\tau) \tag{1}$$

where K is a lidar constant independent of height, $O(z)$ is an overlap function, $\beta(z)$ is a backscatter coefficient at height z, and τ is an optical thickness of the atmosphere up to height z (Wandinger, 2006). The optical thickness is defined as follow:

13

$$\tau = \int_0^z \alpha(z')\, dz' \tag{2}$$

where α(z) is an extinction coefficient at height z.

The ceilometer outputs a vertical profile of attenuated backscatter coefficients with a height resolution of 10 m every 6 sec. The height range of the profile is from 10 m to 15400 m. The attenuated backscatter coefficient is calculated from the intensity P(z) by the vender software of Vaisala. The attenuated backscatter coefficient β'(z) at height z is defined and derived from the Eq. (1) as follows.

$$\beta'(z) = \beta(z)\,\exp(-2\tau) = \frac{P(z)\,z^2}{K\,O(z)} \tag{3}$$

The attenuated backscatter coefficient is the backscatter coefficient taking account of the attenuation of an emitted laser pulse and the backscatter light in the atmosphere. The influence of water vapor on the attenuated backscatter coefficients obtained from the ceilometer is probably small because of low relative humidity in the Gobi Desert as discussed in Jin et al. (2015). The average of the data for one minute or for 15 minutes and 30 m were used in this study.

The observation data of the ceilometer CL51 includes the information of the instrument status such as laser temperature and the contamination degree of the observation window. The observation window should be cleaned manually when the contamination degree is not improved though the window blower works for a long time.

2.1.5 Analysis method

The major scatterers over the Gobi Desert in spring are dust, clouds, and precipitation. Their detection and distinction are based on the magnitude, height, and distribution of attenuated backscatter coefficients. During this dust event, the threshold of attenuated

14

backscatter coefficient for distinguishing dust and the others was about 9×10^{-3} km^{-1} sr^{-1}. In addition, relative humidity in a region of large attenuated backscatter coefficients supports their distinction. Natsagdorj et al. (2003) showed that relative humidity was low in most dust storms in Mongolia.

Optical parameters such as aerosol extinction coefficients and optical thickness were derived from the attenuated backscatter coefficients observed by the ceilometer. First, aerosol backscatter coefficients were calculated from the attenuated backscatter coefficients based on the Fernald's forward inversion method using two components of particles and molecules (Fernald, 1984). In this calculation, the lidar ratio (the ratio of extinction coefficient to backscatter coefficient) for aerosols was assumed to be 50 sr because the primary target of this study is Asian dust. This value was based on the observation results of the previous studies summarized in Cattrall et al. (2005). The boundary was set to the lowest height (10 m AGL) of the observation data. It was assumed that the optical thickness between the ground and the lowest height was unity (1.0), which means that the attenuated backscatter coefficient equaled to the total backscatter coefficient at the lowest height. The vertical profile of molecular densities was obtained from the U.S. standard atmosphere model of 1976 (NOAA et al., 1976). Molecular backscatter coefficient was calculated by means of Hostetler et al. (2006). Secondly, aerosol extinction coefficients were calculated from the aerosol backscatter coefficients with an aerosol lidar ratio of 50 sr. Finally, aerosol optical thickness (AOT) was derived from the integration of the aerosol extinction coefficients below a height of 4 km. If there was a cloud below a height of 4 km, the top height of the integration was changed to the base height of the cloud.

The overlap function O(z) used in the ceilometer and its calculation method are unknown to users. Wiegner et al. (2014) reported that the observation data below 60 m of a ceilometer CL51 were not reliable because its overlap function was incomplete in this range. Therefore,

the attenuated backscatter coefficients below 60 m are not shown in the figures of this thesis.

2.1.6 Data correction using a sunphotometer

The lidar constant K of the ceilometer is determined by Vaisala. The value and its calculation method are also unknown to users. Jin et al. (2015) pointed out that the ceilometer underestimated attenuated backscatter coefficients by comparing the ceilometer with a dual-wavelength lidar in Tsukuba, Japan. In the present study, the lidar constant of the ceilometer in Dalanzadgad was corrected by sunphotometer near the ceilometer. The sunphotometer was installed by NASA in 1997 and belongs to the AERONET (AErosol RObotic NETwork) (Holben et al., 2001). The attenuated backscatter coefficients observed by the ceilometer were corrected by a factor of 1.43 so that the AOT derived from the ceilometer with an aerosol lidar ratio of 50 sr corresponds to the AOT at a wavelength of 910 nm obtained from the AERONET sunphotometer observation during a dust storm on 22 May 2013. The corrected attenuated backscatter coefficients were used to derive aerosol extinction coefficients and AOT.

Figure 2.1: Satellite image in Dalanzadgad obtained from Google Earth (access on 8 January 2018). The red circle indicates the location of the Dalanzadgad Meteorological Observatory. The horizontal scale bar is shown at the lower right of the image.
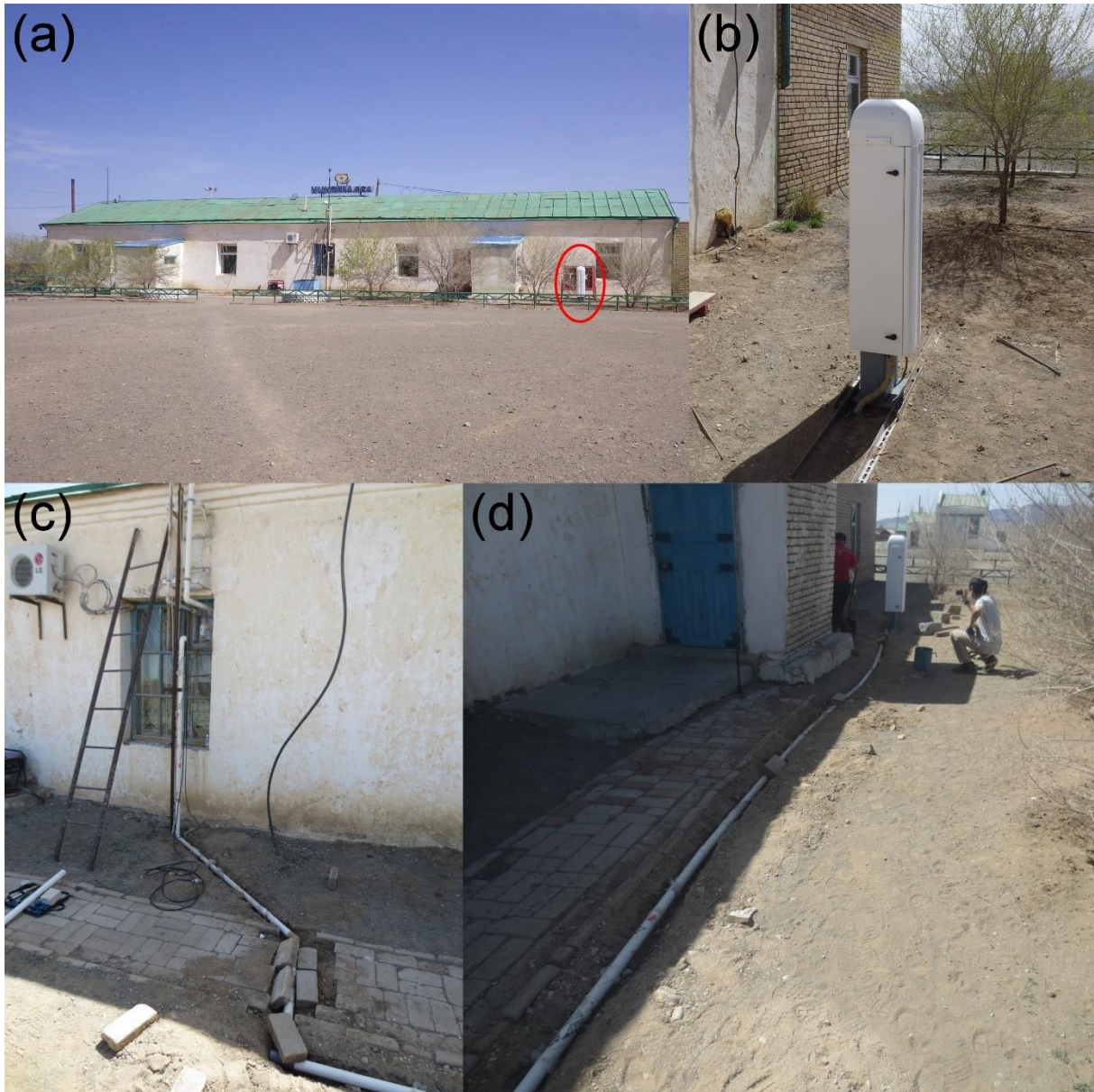
Figure 2.2: (a) Main building of the Dalanzadgad Meteorological Observatory and (b) the ceilometer (Vaisala CL51) used in this study (taken by the author on 5 May 2015). The red circle in panel (a) indicates the ceilometer, which is located in front of the main building. (c–d) The route of the power and data cables of the ceilometer (taken by the author on 29 April 2013). The cables run through the white pipes from the ceilometer to the main building.
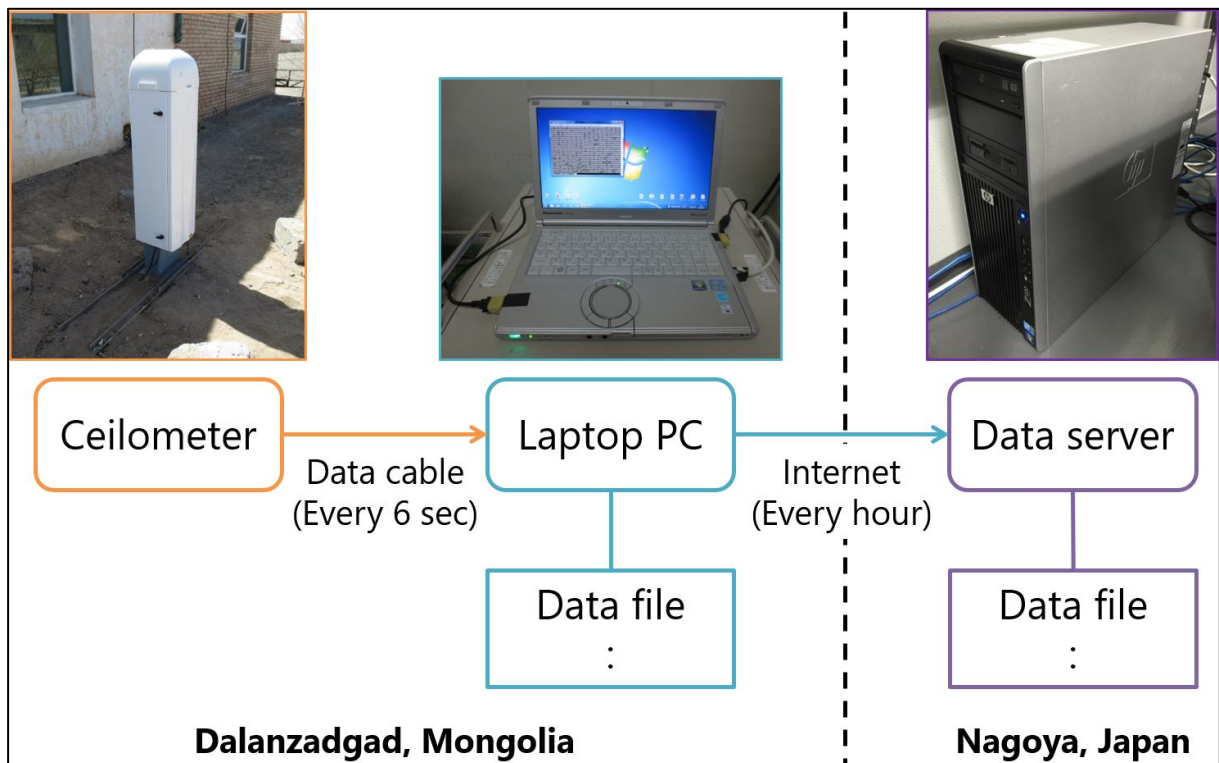
Figure 2.3: Automated observation system for the ceilometer installed in Dalanzadgad. The laptop PC and the data server are located in the Dalanzadgad Meteorological Observatory and Nagoya University, respectively. The arrows indicate the flow of ceilometer observation data from the ceilometer to the laptop PC and the data server through the data cable and the Internet.
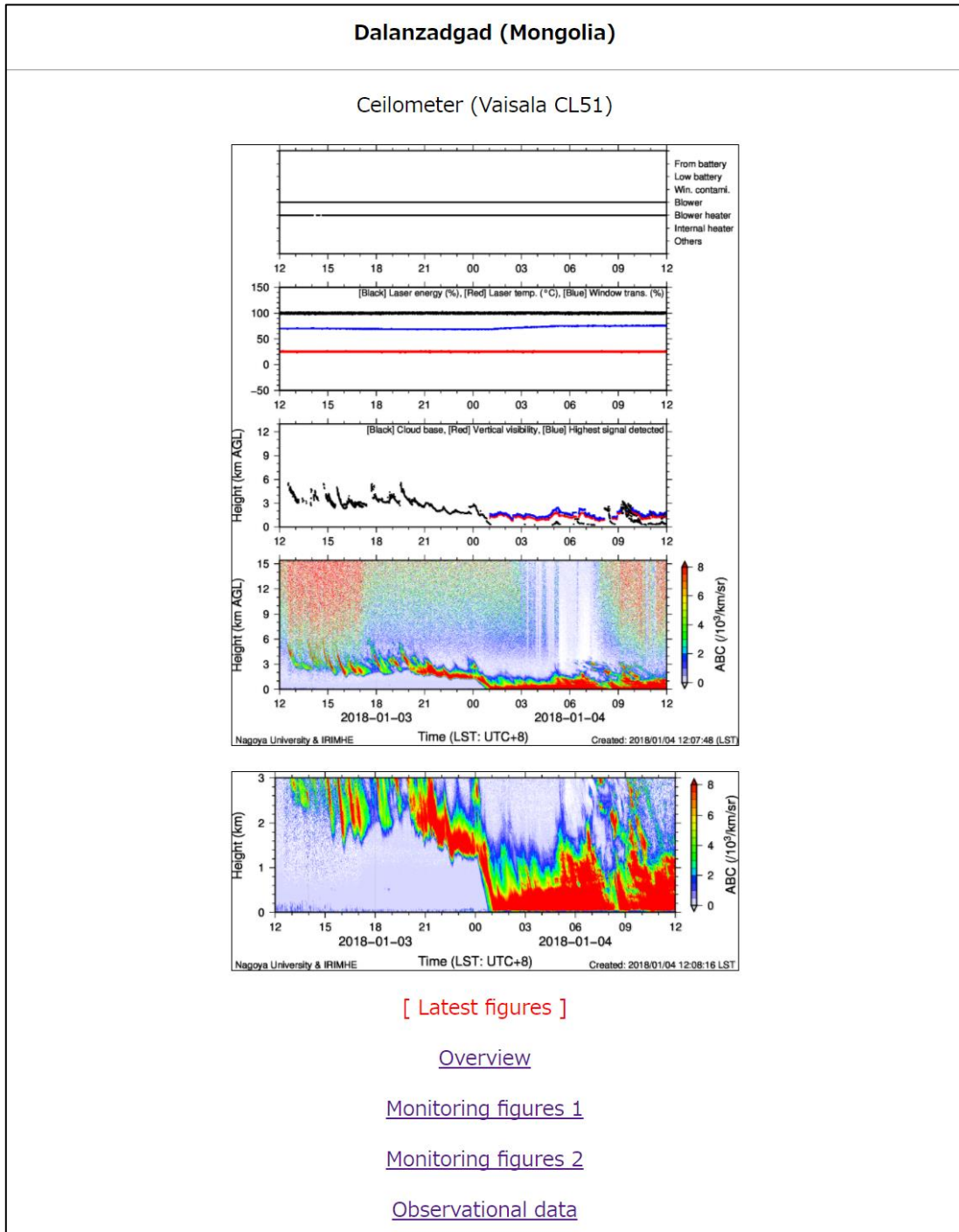
Figure 2.4: Website of the ceilometer observation (access on 4 January 2018), which is published on the web server of Prof. Kai's Laboratory in Nagoya University (http://env728.env.nagoya-u.ac.jp/CL51/). On this day, it was snowy in Dalanzadgad, and the snowfall is shown by large attenuated backscatter coefficients on the ground ($>3.0 \times 10^{-3}$ /km/sr, green to red).

2.2 AD-Net lidar observations in Sainshand and Zamyn-Uud, Mongolia

Lidar observations have been conducted in the eastern part of the Gobi Desert. These lidars are operated by the National Institute for Environmental Studies (NIES), Japan, and the National Agency for Meteorology and Environmental Monitoring (NAMEM), Mongolia. These observations belong to the Asian Dust and Aerosol Lidar Observation Network (AD-Net), which is a widespread lidar network in East Asia (Sugimoto et al., 2008).

2.2.1 Observation site

The two AD-Net lidars in the eastern part of the Gobi Desert are installed in Sainshand (44.87°N, 110.12°E, 937 m ASL; S in Fig. 1.5) and Zamyn-Uud (43.72°N, 111.90°E, 962 m ASL; Z in Fig. 1.5), Mongolia. The Gobi Desert lidar network consists of the ceilometer in Dalanzadgad (D) and the AD-Net lidars in Sainshand (S) and Zamyn-Uud (Z). The distances among these observation sites are 480 km (D–S), 600 km (D–Z), and 190 km (S–Z).

2.2.2 Observation instrument

The AD-Net lidars are dual-wavelength polarization-sensitive backscatter lidars (Fig. 2.5). The lidars utilize an Nd:YAG laser with the energy of 50 mJ as the light source. The laser wavelengths are 532 and 1064 nm, the pulse repetition rate is 10 Hz, and the pulse energy is 50 mJ. The polarization of backscatter light is measured at a wavelength of 532 nm. The laser beams of 532-nm and 1064-nm wavelengths are emitted upward vertically. A telescope with a diameter of 20 cm is used in each lidar to collect backscatter light.

2.2.3 Observation data

The observation data includes the vertical profiles of attenuated backscatter coefficients at both wavelengths and volume depolarization ratio at a wavelength of 532 nm up to a height

21

of 18 km. The time and height resolutions are 15 min and 30 m, respectively. The volume depolarization ratio δ, which is the depolarization ratio containing the effects of both aerosols and atmospheric molecules, is defined as follows:

$$\delta = P_\perp / P_\parallel \tag{4}$$

where $P_\perp$ and $P_\parallel$ are the intensity of the backscatter light of perpendicular and parallel components, respectively (Shimizu et al., 2004). If the scatterer is spherical, the depolarization ratio is almost zero. The more nonspherical the scatterer is, the larger the depolarization ratio becomes. The typical nonspherical scatterers are mineral dust and ice cloud. Shimizu et al. (2004) identified the depolarization ratio exceeding 0.1 as mineral dust.The volume depolarization ratio is an index of particle sphericity. This value is zero for a spherical particle and increases with non-sphericity.

2.2.4 Analysis method

We calculated volume color ratio, a relative index of particle size, by dividing the 1064-nm attenuated backscatter coefficient by the 532-nm one. This value increases as particle size increases. The 532-nm attenuated backscatter coefficient near the ground in Zamyn-Uud was calibrated for an incomplete overlap function by using data on 24 May 2013, when the atmosphere was clean following the dust event. Shimizu et al. (2010) mentioned that the final results below 120 m altitude are not published in further analysis because the accuracy of retrieved data in the lower atmosphere is unknown. Therefore, the attenuated backscatter coefficients and volume depolarization ratio below 120 m AGL are not shown in figures in the present study. Optical parameters such as aerosol extinction coefficients and optical thickness were calculated from the 532-nm attenuated backscatter coefficients by using the same method of the ceilometer (see Section 2.1.5).
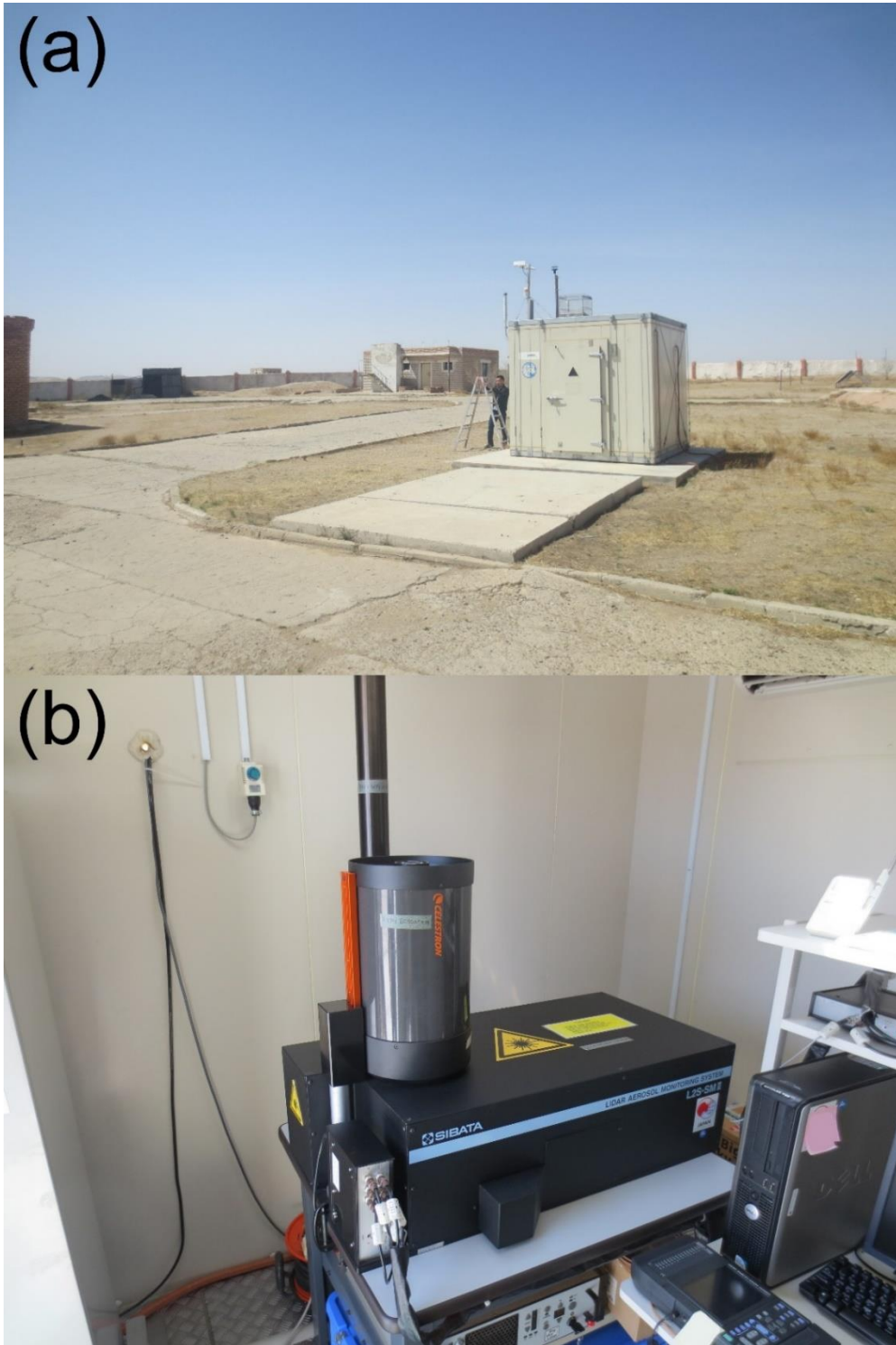
Figure 2.5: (a) Container and (b) instrument of the AD-Net lidar installed in the Sainshand Meteorological Observatory (taken by the author on 29 April 2014).

2.3 Meteorological data

Surface weather charts produced by the Japan Meteorological Agency (JMA) were used. Surface meteorological observational data were obtained from 3-hourly SYNOP reports acquired from the Integrated Surface Database of the National Oceanic and Atmospheric Administration (NOAA), USA (Smith et al., 2011). The SYNOP present weather codes of 06–09, 30–35, and 98 were regarded as dust phenomena (World Meteorological Organization, 2011). A routine radiosonde observation was conducted in Dalanzadgad twice a day. This study used the vertical profiles of potential temperature, relative humidity, and horizontal wind averaged in a height of 100 m from the radiosonde observation data. PM10 and PM2.5 concentrations measured at a height of 4 m in Dalanzadgad by Kosa Monitor of NIES and NAMEM were used. This study used the true color RGB images and NDVI data derived from the MODIS (MODerate resolution Imaging Spectroradiometer) onboard the Terra and Aqua satellites. Three-dimensional gridded meteorological data produced by the National Centers for Environmental Prediction (NCEP) of NOAA were used. The data are NCEP FNL (Final) Operational Global Analysis data of $1º \times 1º$ grids. This product is generated from the global meteorological data of the Global Data Assimilation System (GDAS) using the same model as the NCEP global forecast system. The NCEP FNL data were validated by the radiosonde observation data in Dalanzadgad (Figs. 3.9 and 3.10). These vertical profiles approximately correspond except for detailed variations of the meteorological elements. In addition, trajectory analyses were performed using the Hybrid Single-Particle Lagrangian Integrated Trajectory (HYSPLIT) model provided by the NOAA Air Resources Laboratory (Stein et al., 2015). The GDAS data of $1º \times 1º$ grids were selected as the input meteorological data of the trajectory analyses. The local standard time (LST) of Mongolia, which is 8 hours ahead of the coordinated universal time (UTC), is used in this paper.

3. Results

3.1 Meteorological conditions in Mongolia

Surface weather charts for Mongolia on 22–23 May 2013 are shown in Fig. 3.1. An extratropical cyclone covered central Mongolia at 14 LST on 22 May (Fig. 3.1a) and moved northeastward for the next 18 hours. The center pressure of the cyclone was almost constant at 988 hPa during this period. Warm and cold fronts accompanied the cyclone from 20 LST on 22 May (Figs. 3.1b–3.1d). The cold front extended from the cyclone center to southern Mongolia across the Gobi Desert at 20 LST on 22 May (Fig. 3.1b) and then moved southeastward through the desert at a speed of about 30 km/h. During the movement, it passed through Dalanzadgad between 14 and 20 LST on 22 May, Sainshand between 20 LST on 22 May and 02 LST on 23 May, and Zamyn-Uud between 02 and 08 LST on 23 May.

Figure 3.2 shows the meteorological fields observed around Mongolia at the same time as the second and third weather charts (Figs. 3.1b and 3.1c) obtained from the SYNOP report. At 20 LST on 22 May, the cold air behind the cold front covered central Mongolia (including Dalanzadgad), and the warm air in front of the cold front covered eastern Mongolia (Fig. 3.2a). The wind speeds in central Mongolia were 6–16 m/s, and the strong wind caused dust phenomena along the cold front. At 02 LST on 23 May, the cold air expanded to eastern Mongolia (including Sainshand) while the cold front moved southeastward (Fig. 3.2b). At both these times, the wind directions were between north and northwest in the cold air and between south and west in the warm air. These wind conditions show cold and warm air advections. The cold and warm airflows converged along the cold front.

Figure 3.3 presents meteorological fields at 700 hPa at the same times as in Fig. 3.2 obtained from the NCEP FNL data. The height at 700 hPa is about 1.5–2.0 km above the ground in Mongolia. At both times in Fig. 3.3, updrafts spread in the warm air along the surface cold front. These updrafts were caused by the convergence of the cold and warm air on the ground

25

(Fig. 3.2). Therefore, the warm air on the ground ascended onto the cold air, as shown in the general cold frontal system (e.g., Simpson, 1997; Wallace and Hobbs, 2006).

Figure 3.4 shows the true-color image around Mongolia at 1140 LST on 23 May 2013 obtained from the MODIS of the Terra satellite. The cold front at this time is estimated to have been located a little to the southeast of the one at 08 LST on 23 May. According to this satellite image, a long zonal cloud extended from western Mongolia to southern Mongolia along and behind the cold front. This cloud covered Dalanzadgad and Sainshand. The cloud must have been generated by the updrafts of the warm air indicated in Fig. 3.3, as shown in the general cold frontal system (e.g., Simpson, 1997; Wallace and Hobbs, 2006).
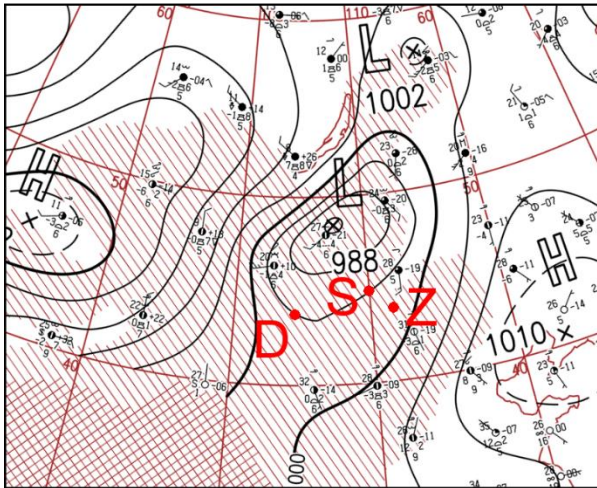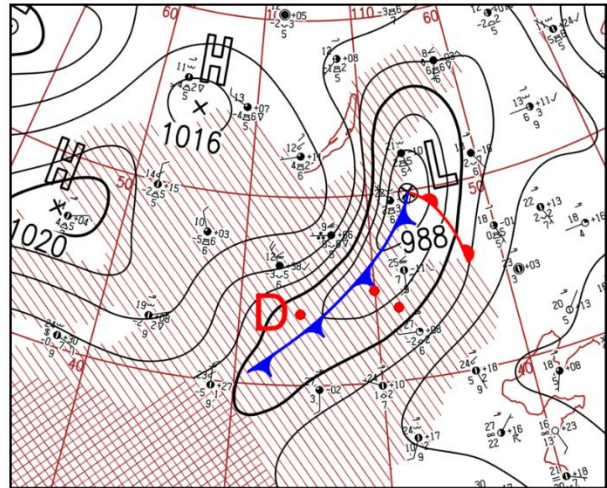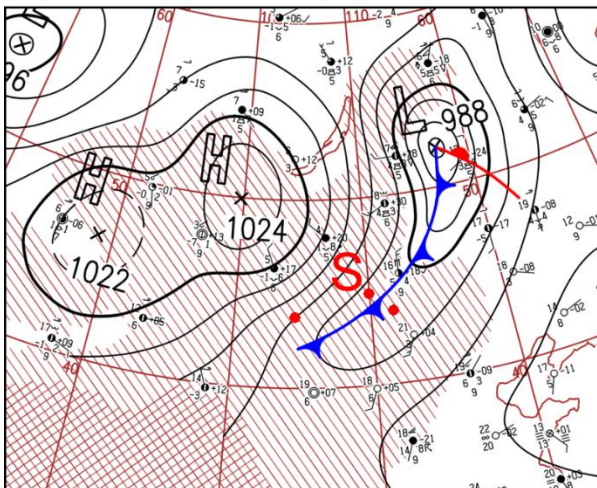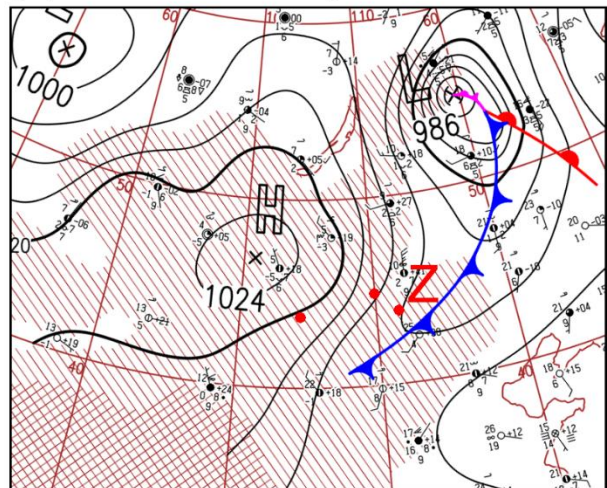
Figure 3.1: Surface weather charts for Mongolia at (a) 14 LST and (b) 20 LST on 22 May and at (c) 02 LST and (d) 08 LST on 23 May 2013 provided by JMA. The red dots show the locations of Dalanzadgad (D), Sainshand (S), and Zamyn-Uud (Z). The sparse and dense red-shaded areas indicate altitudes of more than 1500 and 3000 m above sea level, respectively.
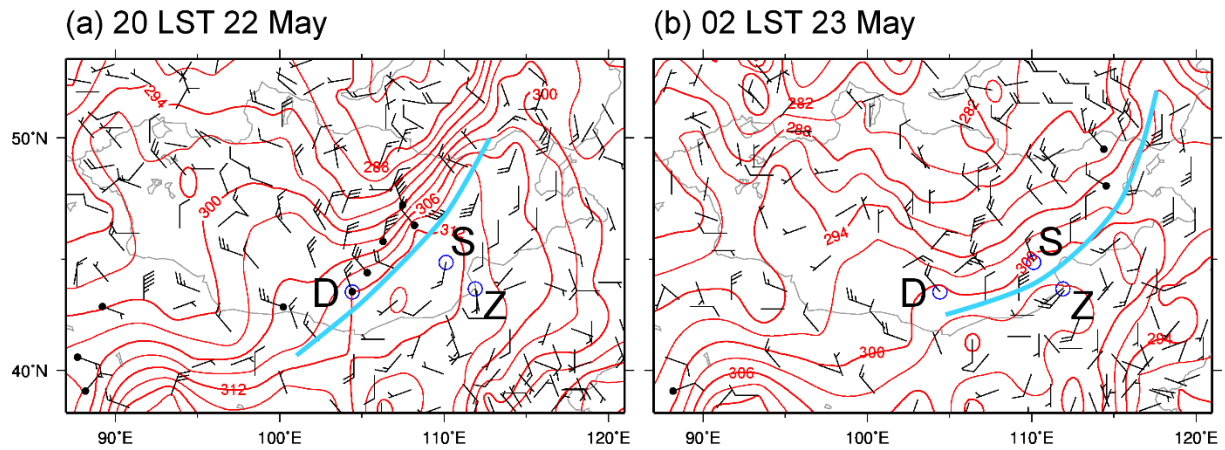
Figure 3.2: Potential temperature (red contours; every 3 K), surface wind (barbs), and dust phenomena (black dots) observed at (a) 20 LST on 22 May and (b) 02 LST on 23 May 2013 obtained from the SYNOP report. The half and full barbs represent the wind speeds of 2 and 4 m/s, respectively. The blue lines indicate the cold fronts transcribed from the weather charts (Figs. 3.1b and 3.1c). The blue circles with the letters D, S, and Z show the locations of Dalanzadgad, Sainshand, and Zamyn-Uud, respectively.
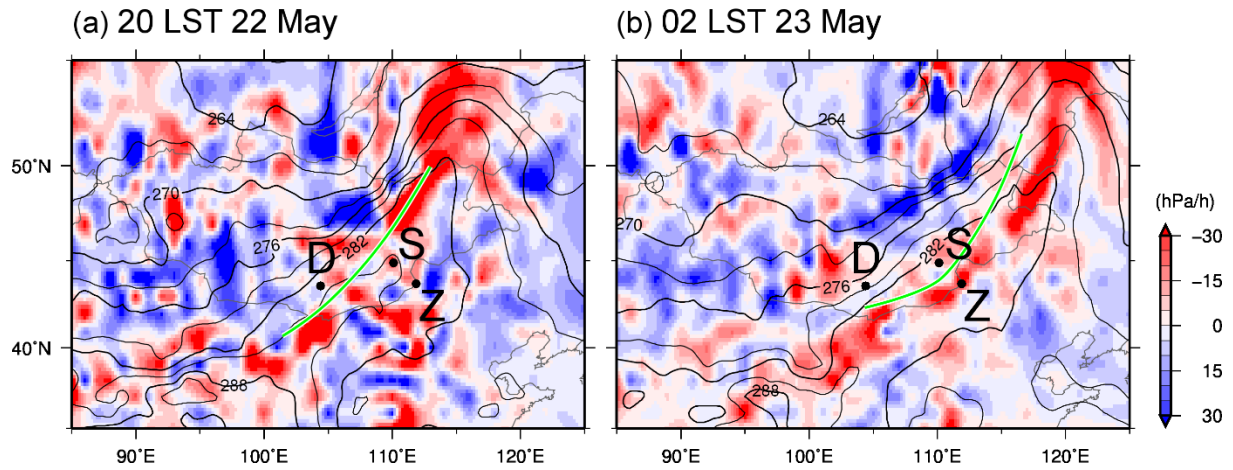
Figure 3.3: Temperature (contours; every 3 K) and vertical velocity (color) at 700 hPa at (a) 20 LST on 22 May and (b) 02 LST on 23 May 2013 obtained from the NCEP FNL data. For the vertical velocity, a negative value (red) indicates an updraft, whereas a positive value (blue) indicates a downdraft. The green lines indicate the surface cold fronts transcribed from the weather charts (Figs. 3.1b and 3.1c). The black dots with D, S, and Z show the locations of Dalanzadgad, Sainshand, and Zamyn-Uud, respectively.
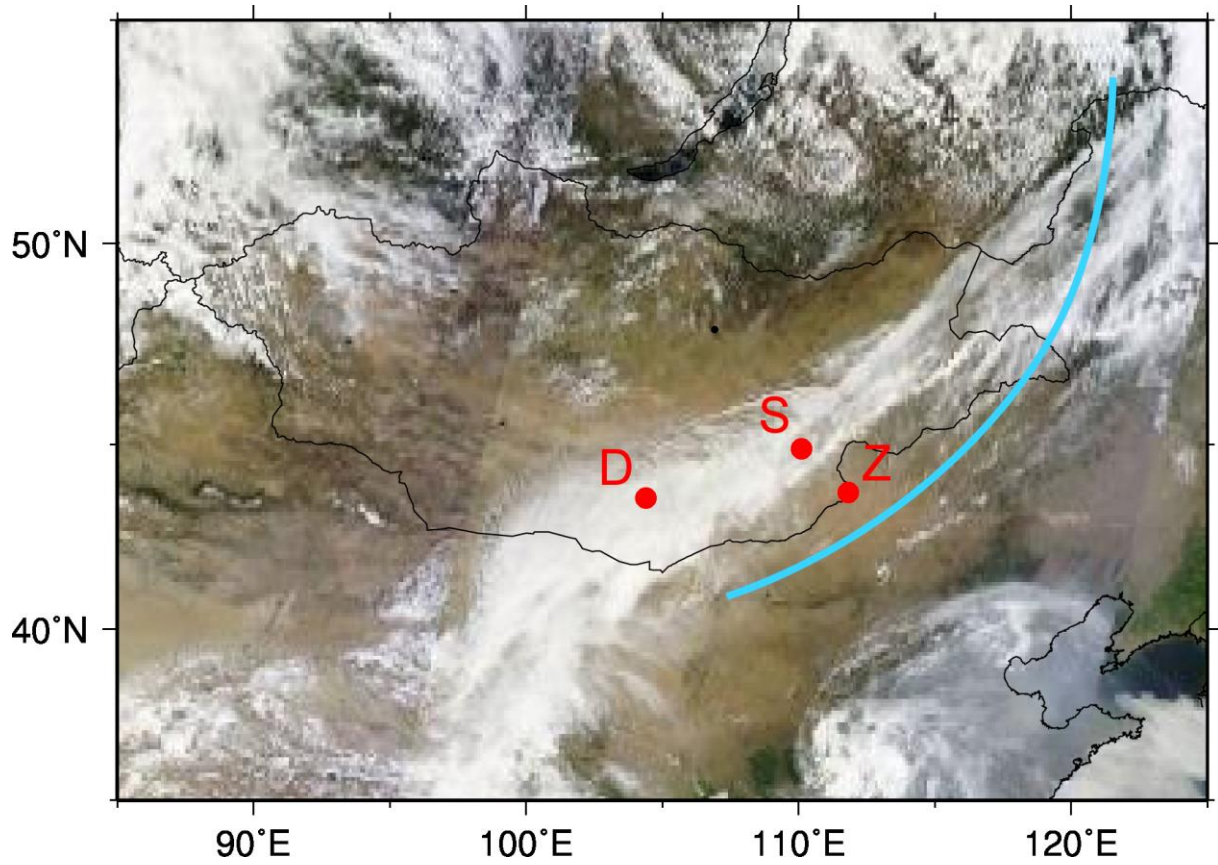
Figure 3.4: True-color image around Mongolia at 1140 LST on 23 May 2013 obtained from the MODIS of the Terra satellite. The blue line shows the cold front transcribed from the surface weather chart at 08 LST on 23 May (Fig. 3.1d). The red dots with D, S, and Z indicate the location of Dalanzadgad, Sainshand, and Zamyn-Uud, respectively.

3.2 Results in Dalanzadgad, located in the central part of the Gobi Desert

In this sub-section, various data in Dalanzadgad from 12 LST on 22 May to 09 LST on 23 May 2013 are described. Figure 3.5 indicates the temporal variations in the surface meteorological observation data. Figure 3.6 presents the time series of the PM10 and PM2.5 concentrations near the ground. Figure 3.7 shows the time-height cross sections of the ceilometer observation result and meteorological conditions obtained from the NCEP FNL data. Figure 3.8 shows the time-height cross section of the corrected aerosol extinction coefficients derived from the ceilometer observation result and time series of the aerosol optical thickness (AOT) calculated from the corrected aerosol extinction coefficients. Figures 3.9 and 3.10 indicate the vertical profiles of the radiosonde observation data and the NCEP FNL data at 20 LST on 22 May and 08 LST on 23 May. In these results, four characteristics were discerned (regions A–D) and are discussed as follows.

Region A of medium to large attenuated backscatter coefficients ($>1.0 \times 10^{-3}$ /km/sr, light blue to red) shows a dust storm between the ground and a height of 1.6 km from 14 LST on 22 May to 02 LST on 23 May (Fig. 3.7a). The AOT of the dust storm ranged from 0.2 to 0.7 (Fig. 3.8b). The PM10 and PM2.5 concentrations near the ground increased from their background values during the dust storm and had a peak (119 and 76 $\mu g/m^3$, respectively) at 21–22 LST on 22 May (Fig. 3.6). During the dust storm, the relative humidity was 11–14% (Fig. 3.5c), and the wind speed was 6–10 m/s (Fig. 3.5d). This strong wind raised the dust from the desert surface. In the dust storm at 20 LST on 22 May, the potential temperature and relative humidity were almost constant with height (314–316 K and 30 %) (Fig. 3.9a). The wind speed increased from 10 m/s near the ground to 21 m/s at a height of 0.6–0.8 km, and decreased to 10 m/s above a height of 1.0 km (Fig. 3.9b). The wind direction was northwest below a height of 0.8 km, and rotated to west at a height of 0.8–1.8 km. The atmospheric neutral stability and the strong wind show that vertical and horizontal mixing was active because of turbulence in the dust storm.

31

The sea level pressure increased by 23.3 hPa from 17 LST on 22 May to 08 LST on 23 May (Fig. 3.5a). The temperature decreased from 28.9 °C at 17 LST on 22 May to 9.4 °C at 08 LST on 23 May (Fig. 3.5b). Hence, the cold front (Fig. 3.1) passed between 17 and 20 LST on 22 May, and the cold air (Fig. 3.2) started to advect on the ground during the dust storm.

Judging from the potential temperature and wind conditions, the vertical structure of the cold air is shown by region B under the dotted line in Fig. 3.7b. The sloping top height between 20 LST on 22 May and 01 LST on 23 May was the cold frontal surface. The top height of the cold air was about 1.4 km at 02 and 08 LST on 23 May. In particular, the top height at 08 LST corresponds to the cloud base height observed by the ceilometer (Fig. 3.7a). The potential temperature was 301 K at 02 LST and 294–298 K at 08 LST on 23 May (Fig. 3.7b). The wind directions in and above the cold air were northeast and west, respectively. According to the radiosonde observation at 08 LST on 23 May, the wind direction was east near the ground, gradually rotated to northwest at a height of 0.2–1.0 km, and suddenly changed to southwest at a height of 1.3–1.4 km (Fig. 3.10b). Most of the cold air indicates small attenuated backscatter coefficients ($<0.5 \times 10^{-3}$ /km/sr, light purple) from 2230 LST on 22 May (Fig. 3.7a), where little dust was floating. This is also shown by the low PM10 and PM2.5 concentrations (<10 μg/m^3) after 02 LST on 23 May (Fig. 3.6). The leading edge of the cold air was occupied by the dust storm.

Region C of medium to large attenuated backscatter coefficients ($>1.0 \times 10^{-3}$ /km/sr, red) shows clouds over a height of 1.6 km between 02 and 07 LST on 23 May (Fig. 3.7a). It is likely that the clouds were generated by the updraft of the warm air (Fig. 3.3), as a general cold frontal system (e.g., Simpson, 1997; Wallace and Hobbs, 2006). According to the radiosonde observation at 08 LST on 23 May, the relative humidity in a cloud was almost 100% at 1.2–2.2 km (Fig. 3.10b). Precipitation is shown by the region of middle to large attenuated backscatter coefficients ($>1.0 \times 10^{-3}$ /km/sr, light blue to red) under the clouds between 05 and 07 LST on

23 May. The precipitation led to the increase in relative humidity at 08 LST on 23 May (Fig. 3.5c).

Region D, which is indicated by medium attenuated backscatter coefficients ($1.0–1.4 \times 10^{-3}$ /km/sr, light blue) at a height of $0.9-1.6$ km between 22 LST on 22 May and 00 LST on 23 May, shows a dust layer (Fig. 3.7a). The thickness of the dust layer ranged from 0.2 to 0.5 km. According to the time-height cross section of aerosol extinction coefficients, the dust layer was connected with the dust storm (Fig. 3.8a). Because the dust layer was located over the cold frontal surface, the dust was probably transported from the dust storm by the updraft of the warm air shown in Fig. 3.3. This upward transport of the dust layer will be discussed in Section 4.1 by using trajectory analysis.
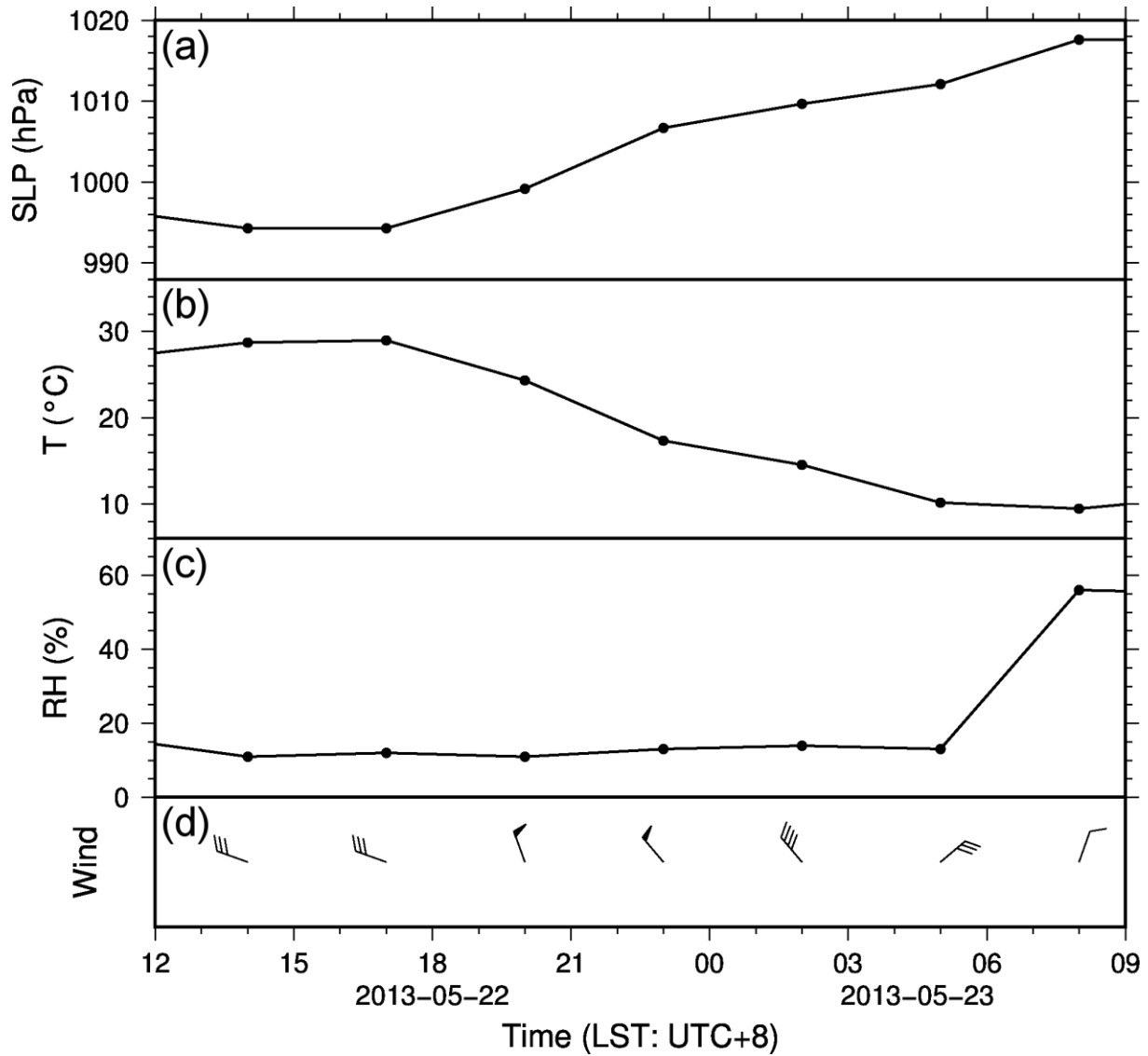
Figure 3.5: Time series of the (a) sea level pressure (SLP), (b) temperature (T), (c) relative humidity (RH), and (d) wind observed in Dalanzadgad from 12 LST on 22 May to 09 LST on 23 May 2013. The half and full barbs and the pennants represent the wind speeds of 1, 2, and 10 m/s, respectively.
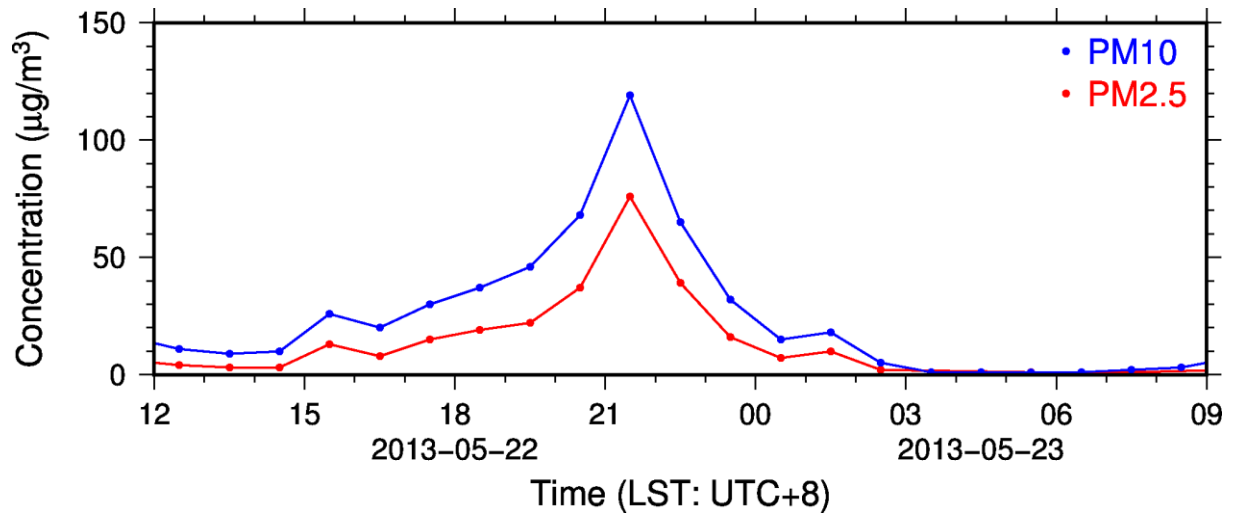
Figure 3.6: Time series of the hourly averaged PM10 (blue line) and PM2.5 (red line) concentrations measured at a height of 4 m in Dalanzadgad from 12 LST on 22 May to 09 LST on 23 May 2013.
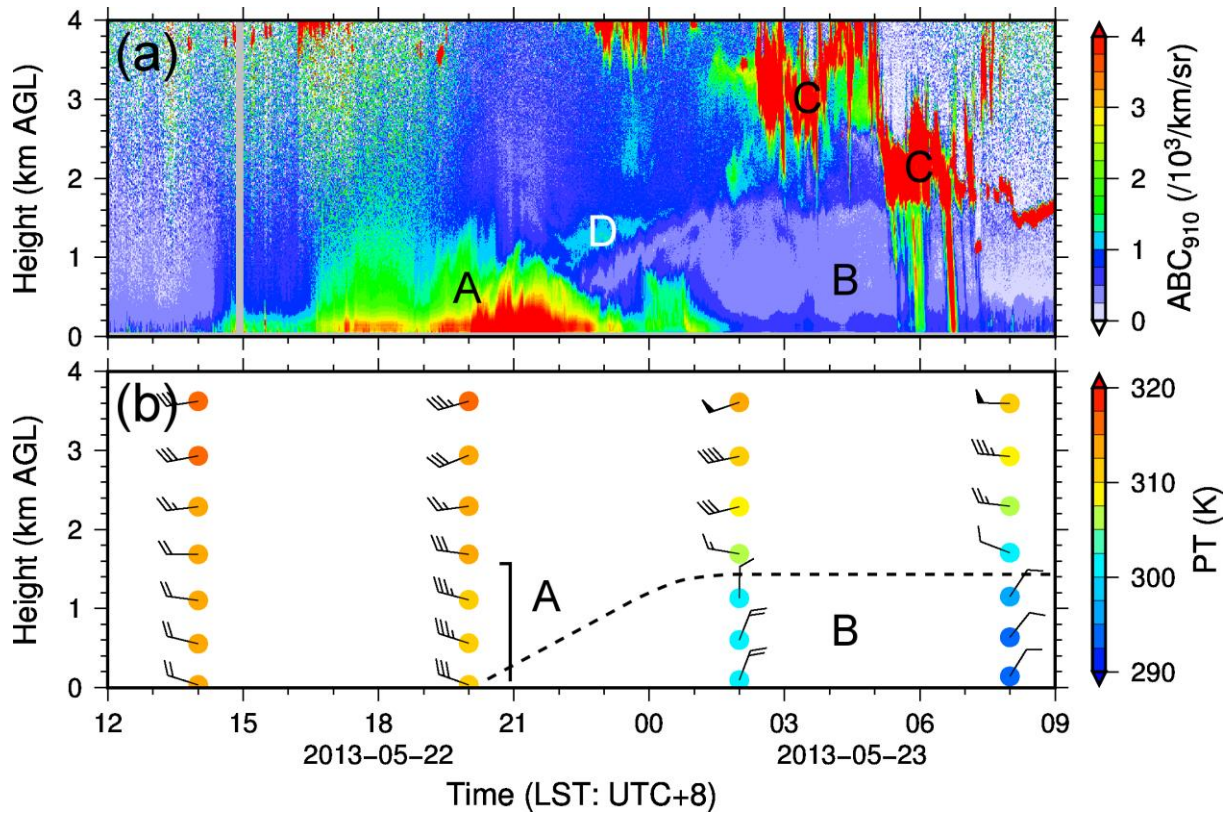
Figure 3.7: Time-height cross sections of the (a) 910-nm attenuated backscatter coefficient (ABC) observed by the ceilometer and (b) potential temperature (PT) and horizontal wind obtained from the NCEP FNL data for Dalanzadgad during the same period as in Fig. 3.5. The half and full barbs and pennants represent the wind speeds of 2, 4, and 20 m/s, respectively. Regions A–D correspond to a dust storm, cold air, clouds, and a dust layer, respectively. The dotted line represents the top of the cold air.
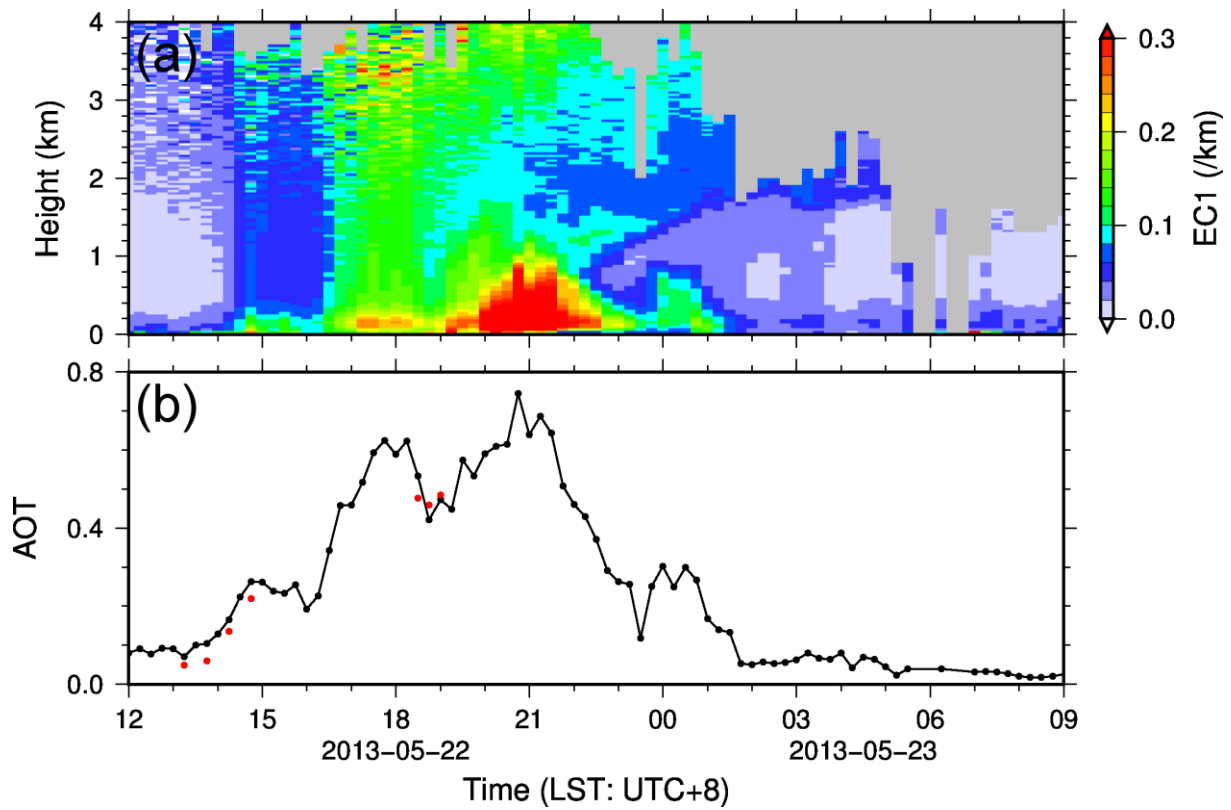
Figure 3.8: (a) Time-height cross section of the aerosol extinction coefficients (EC1) derived with an aerosol lidar ratio of 50 sr from the attenuated backscatter coefficients which were observed by the ceilometer in Dalanzadgad during the same period as in Fig. 3.5 and corrected by a factor of 1.43. The gray areas indicate clouds, precipitation, or calculation error. (b) Time series of the aerosol optical thickness (AOT) calculated from the aerosol extinction coefficients shown in panel A (black line and dots), and the AOT at a wavelength of 910 nm obtained from the AERONET sunphotometer near the ceilometer (red dots). The negative values of the AOT derived from the ceilometer were rejected.
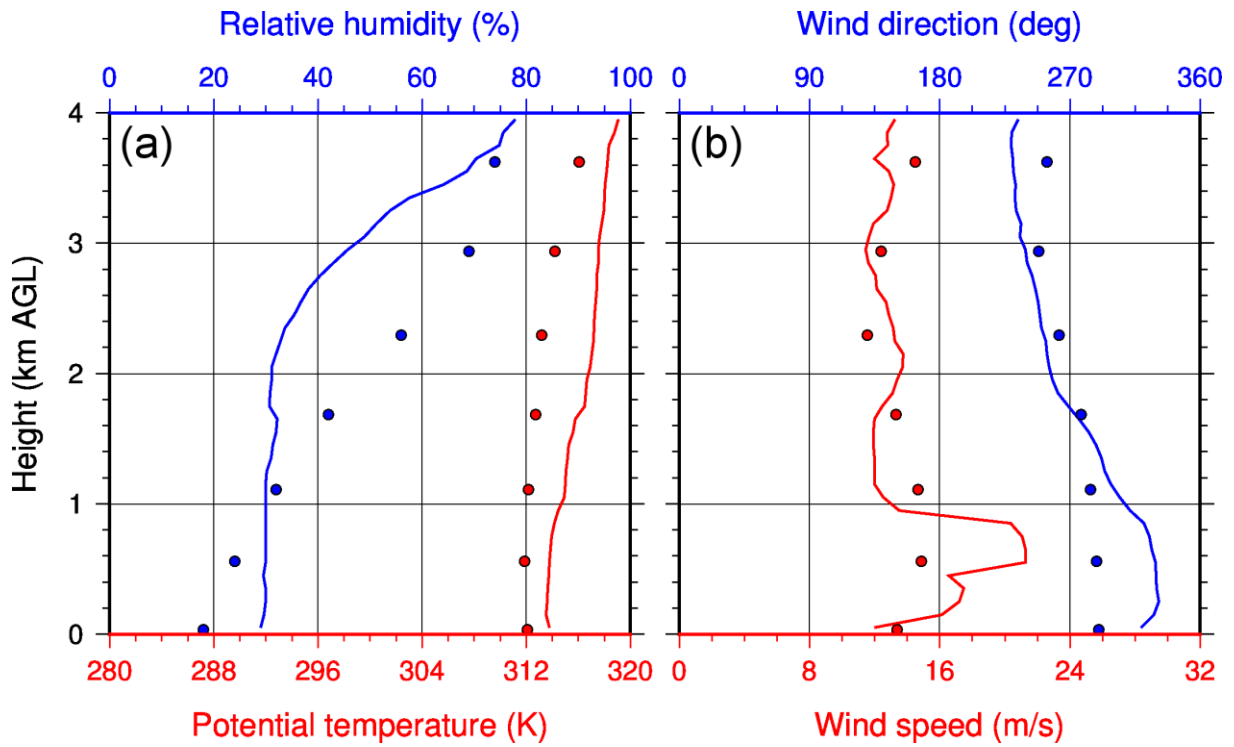
Figure 3.9: Vertical profiles of (a) the potential temperature (red), relative humidity (blue), (b) wind speed (red), and wind direction (blue) in Dalanzadgad at 20 LST on 22 May 2013 observed by radiosonde (lines) and obtained from the NCEP FNL data (44°N, 104°E) (dots). The release time of the radiosonde was 1915 LST.
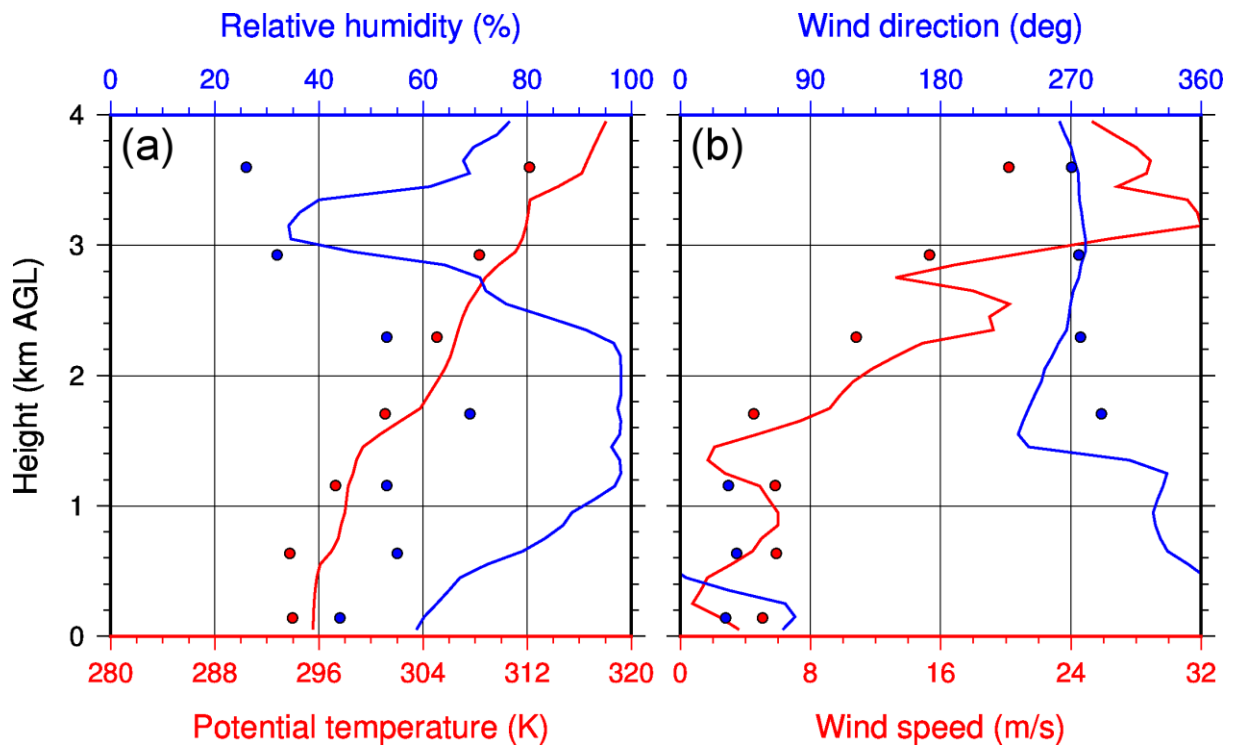
Figure 3.10: Same as Fig. 3.9, but at 08 LST on 23 May 2013. The release time of the radiosonde was 0715 LST.

3.3 Results in Sainshand, located in the eastern part of the Gobi Desert

Figure 3.11 presents the temporal fluctuations in surface meteorological elements observed in Sainshand in the eastern part of the Gobi Desert from 18 LST on 22 May to 15 LST on 23 May 2013. Figures 3.12 and 3.14 show the time-height cross sections of lidar observation results and meteorological conditions obtained from the NCEP FNL data, respectively, for Sainshand during the same period as in Fig. 3.11. Figure 3.13 indicates the time-height cross section of the aerosol extinction coefficients derived from the lidar observation result and time series of the aerosol optical thickness (AOT) calculated from the aerosol extinction coefficients.

Between 22 LST on 22 May and 01 LST on 23 May, a dust storm is shown by region E of large attenuated backscatter coefficients ($>5.5 \times 10^{-3}$ /km/sr, yellow to red) on the ground (Fig. 3.12a). The AOT during the dust storm reached about 1.1 at 2330 LST on 22 May (Fig. 3.13). At 23 LST on 22 May, during the dust storm, the wind speed was 11 m/s (Fig. 3.11d), and the relative humidity was 19% (Fig. 3.11c). In the dust storm, the volume depolarization ratio was 0.2–0.3 (Fig. 3.12b), and the volume color ratio was about 2.0 (Fig. 3.12c).

The sea level pressure increased by 21.3 hPa from 20 LST on 22 May to 08 LST on 23 May (Fig. 3.11a). The temperature dropped from 35.4 °C at 17 LST on 22 May to 13.3 °C at 08 LST on 23 May (Fig. 3.11b). Between 20 and 23 LST on 22 May, the wind direction changed from south to northwest, and the wind speed increased from 6 to 11 m/s (Fig. 3.11d). According to these features, the cold front shown in Fig. 3.1 passed through between 20 and 23 LST on 22 May, and the cold air replaced the warm air, as shown in Fig. 3.2.

Judging from the potential temperature and wind conditions, the vertical structure of the cold air is indicated in region F below the dotted line in Fig. 3.14a. The top height was 1.1 km at 02 LST and 1.3 km at 08 and 14 LST on 23 May. The potential temperature was 303–307 K at 02 LST and 295 K at 08 and 14 LST on 23 May. At 08 and 14 LST on 23 May, there was an inversion layer between 1.1 and 1.5 km in height. The wind directions in and above the cold air

were north and west, respectively. The attenuated backscatter coefficients were small ($<2.0 \times 10^{-3}$ /km/sr, blue) in the cold air after the dust storm (region F in Fig. 3.12a), indicating little floating dust.

Region G of medium to large attenuated backscatter coefficients ($>2.0 \times 10^{-3}$ /km/sr, red) shows clouds, which were located around a height of 2–5 km (Fig. 3.12a). Most of the clouds indicate volume depolarization ratios of more than 0.2 (Fig. 3.12b), indicating the presence of ice crystals (Shimizu et al., 2004). The temperatures around the clouds were between 0 and -10 °C according to the NCEP FNL data (not shown). Therefore, it is likely that the dust particles mentioned later worked as ice nuclei, as suggested by Sakai et al. (2003). The volume color ratio in the clouds was 2.0–2.4 (Fig. 3.12c). The region of medium attenuated backscatter coefficients ($2.0–6.0 \times 10^{-3}$ /km/sr, light blue to yellow) under the clouds around 11 LST on 23 May shows precipitation (Fig. 3.12a). In the precipitation, the volume depolarization ratio was about 0.1 (Fig. 3.12b), which is consistent with that reported by Sassen (2006). The volume color ratio of the precipitation was 2.0–3.0 (Fig. 3.12c).

A dust layer is shown by the medium attenuated backscatter coefficients ($2.0–6.0 \times 10^{-3}$ /km/sr, light blue to yellow) in region H (Fig. 3.12a). It extended from the dust layer (region E) to the clouds (region G) over the cold air (region F). It seems that the dust layer was mixed with the clouds. The top height of the dust layer increased from 1.6 km at 22 LST on 22 May to 4.0 km at 04 LST on 23 May. The thickness of the dust layer was between 1.6 and 2.5 km. The AOT for the dust layer was between 0.3 and 0.7 (Fig. 3.13b). In the dust layer, the volume depolarization ratio was 0.1–0.3 (Fig. 3.12b), and the volume color ratio was 1.0–2.0 (Fig. 3.12c). According to the volume color ratio, the dust particles were smaller than the precipitation particles and the ice crystals of the clouds. Vertical velocity represents updraft in the dust layer at 02 LST on 23 May (region H in Fig. 3.14b). Therefore, the dust layer was distributed in the updraft region of the warm air in the cold frontal system.
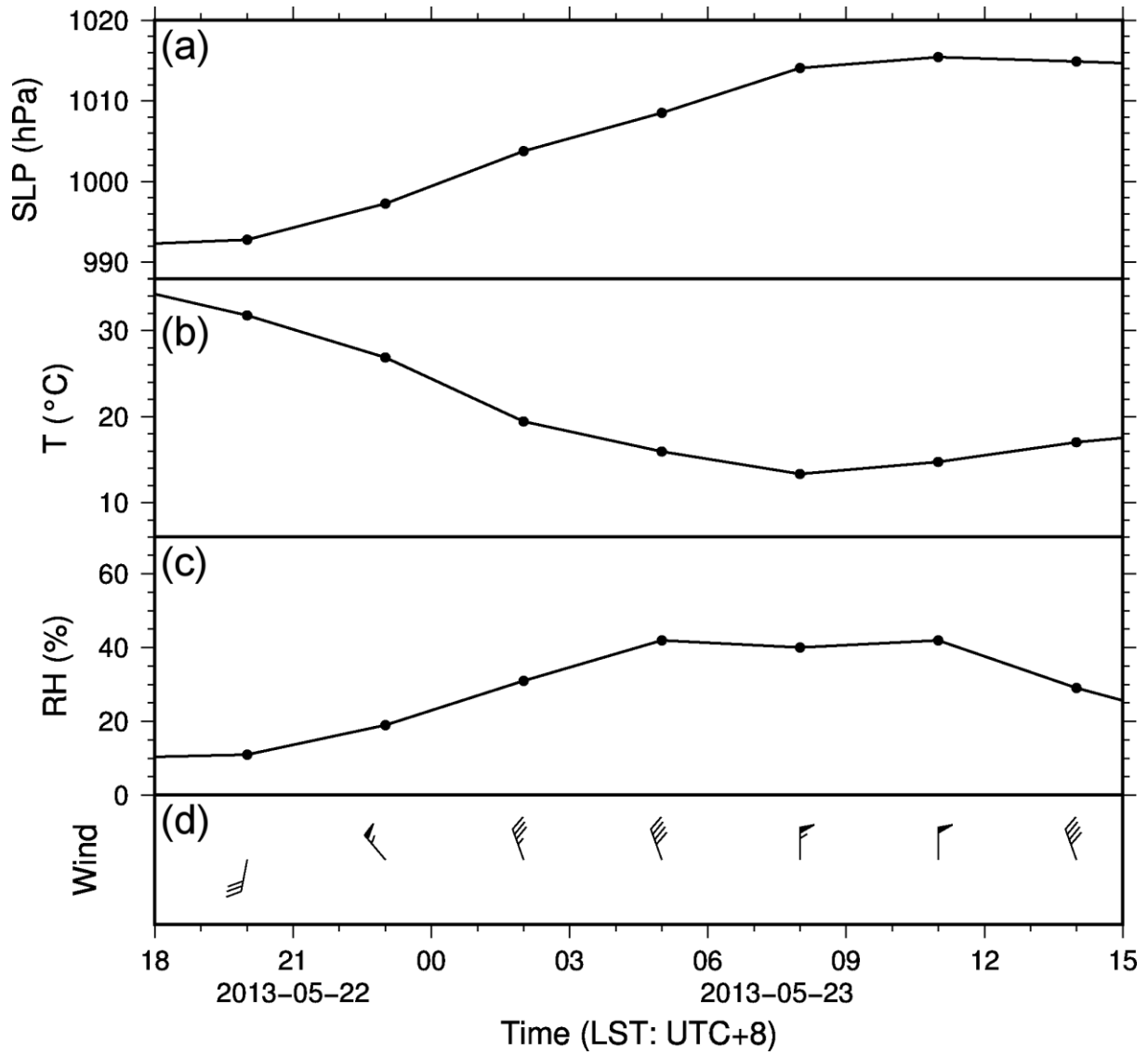
Figure 3.11: Same as Fig. 3.5, except that the location is Sainshand, and the period is from 18 LST on 22 May to 15 LST on 23 May 2013.
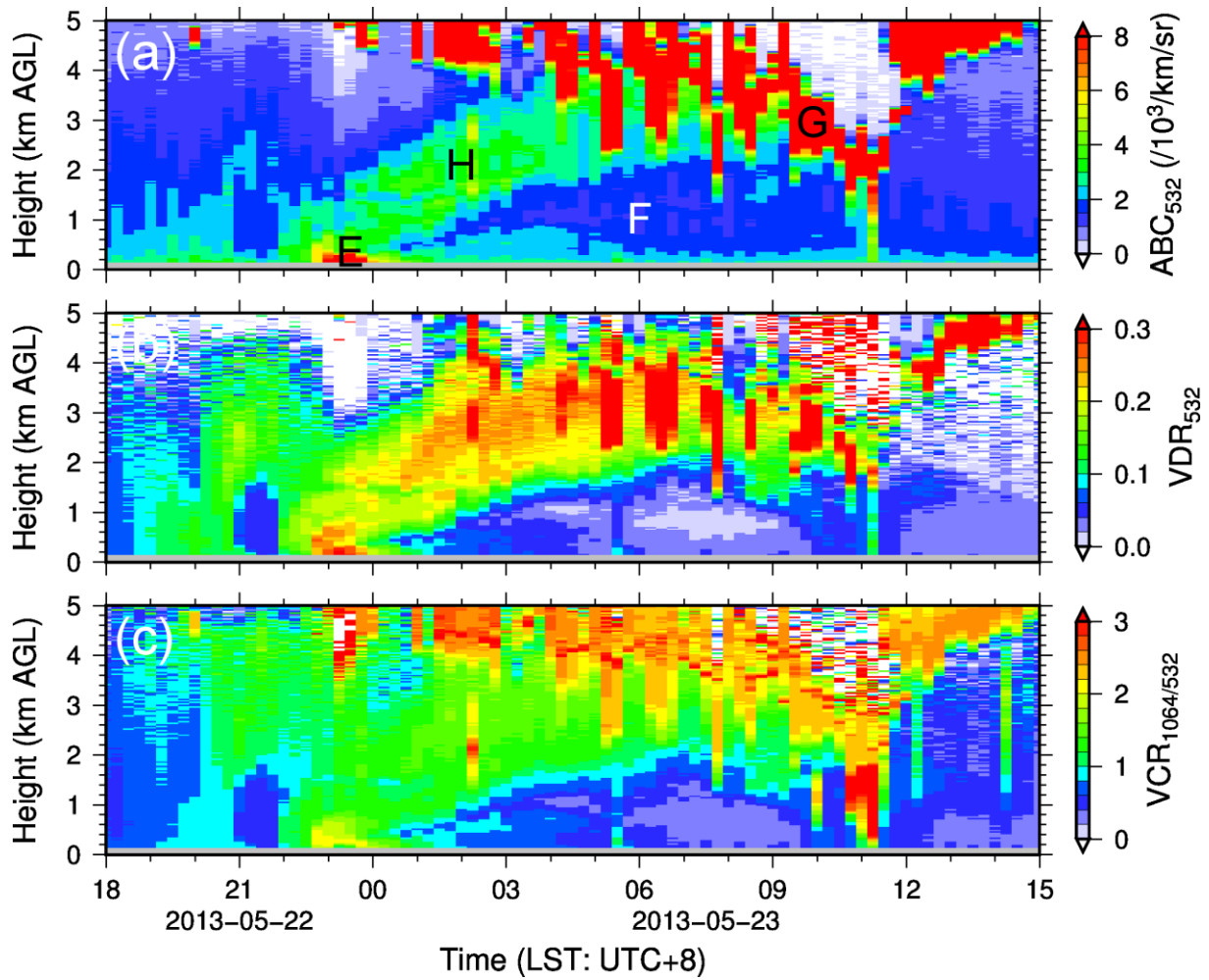
Figure 3.12: Time-height cross sections of the (a) 532-nm attenuated backscatter coefficient (ABC), (b) 532-nm volume depolarization ratio (VDR), and (c) 1064/532-nm volume color ratio (VCR) at a height of 0–5 km observed by the AD-Net lidar in Sainshand during the same period as in Fig. 3.11. Regions E–H correspond to a dust storm, cold air, clouds, and a dust layer, respectively.
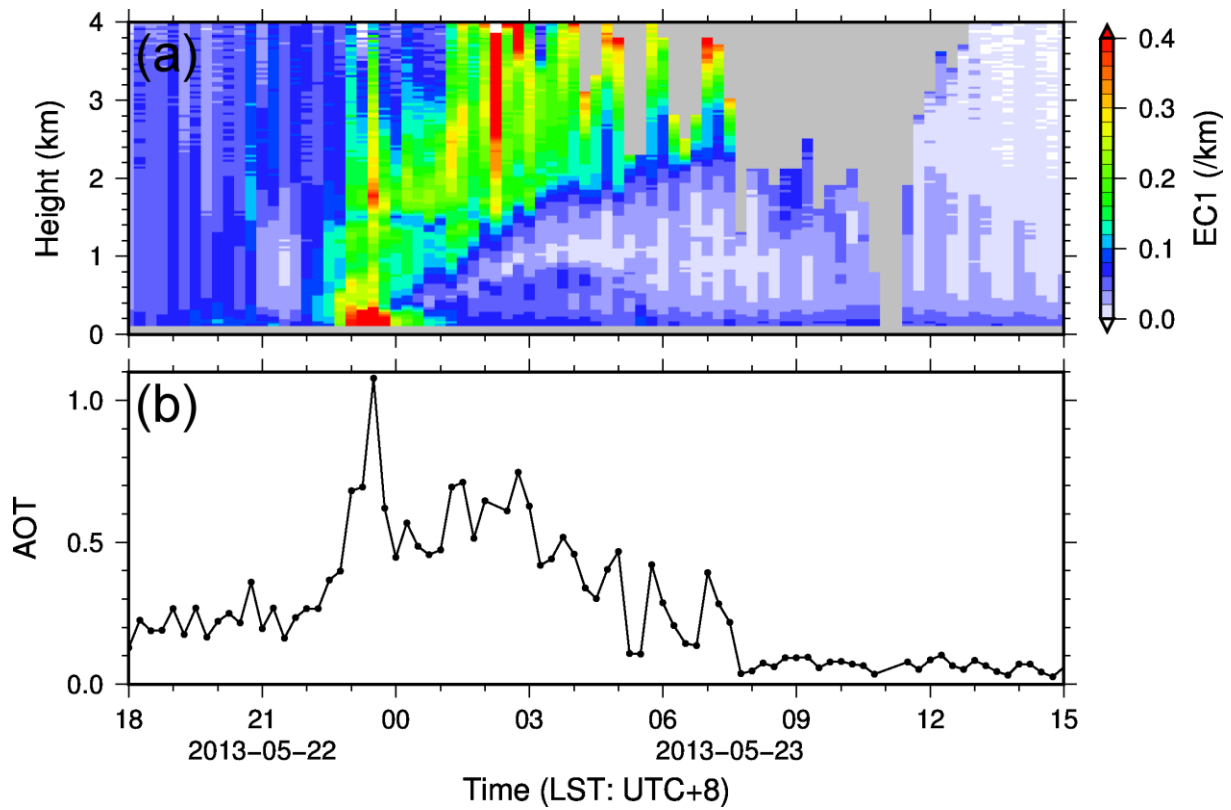
Figure 3.13: (a) Time-height cross section of the aerosol extinction coefficients (EC1) derived from the 532-nm attenuated backscatter coefficients observed by the AD-Net lidar in Sainshand during the same period as in Fig. 3.11 with an aerosol lidar ratio of 50 sr. The gray areas indicate clouds, precipitation, or calculation error. (b) Time series of the aerosol optical thickness (AOT) calculated from the aerosol extinction coefficients shown in panel A. The negative values of the derived AOT were rejected.

44
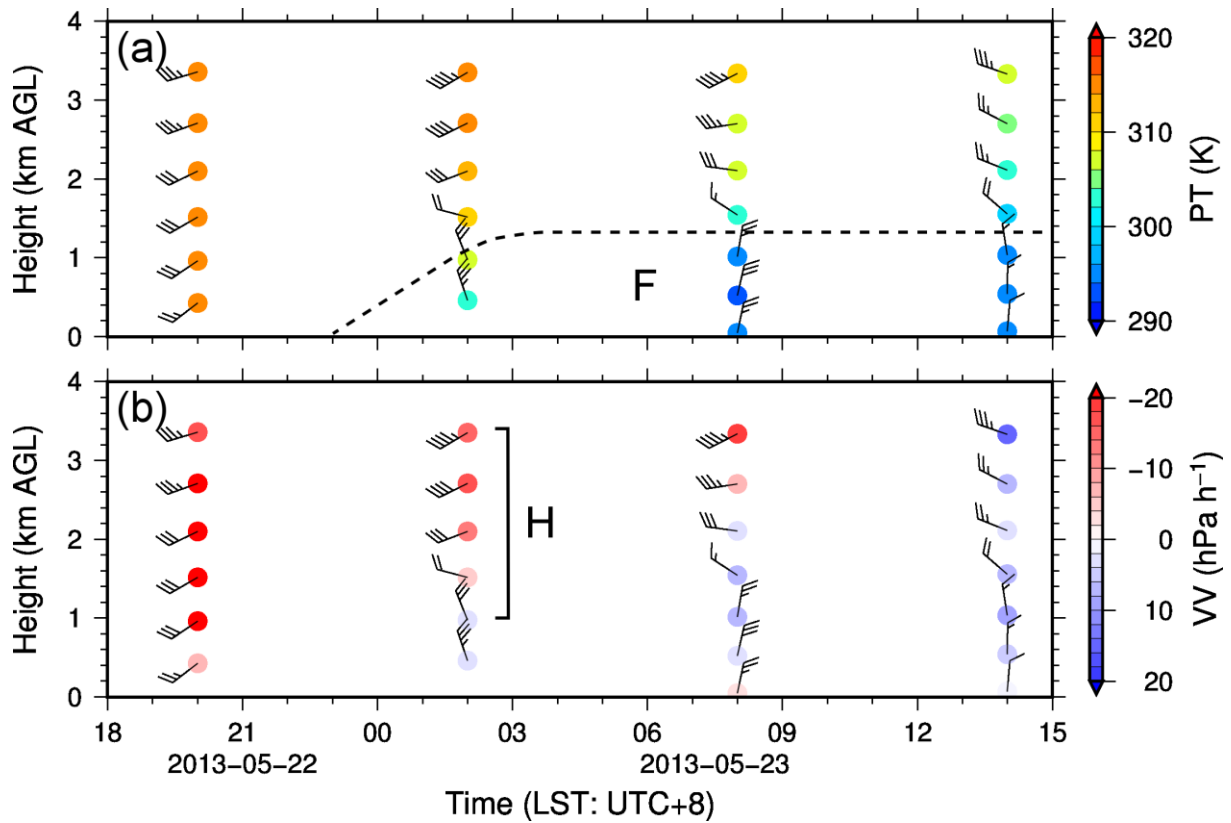
Figure 3.14: Time-height cross sections of the (a) potential temperature (PT) and horizontal wind and (b) vertical velocity (VV) and horizontal wind obtained from the NCEP FNL data for Sainshand during the same period as in Figs. 3.11 and 3.12. The half and full barbs and pennants represent wind speeds of 2, 4, and 20 m/s, respectively. Regions F and H are the same as in Fig. 3.12.

3.4 Results in Zamyn-Uud, located in the eastern part of the Gobi Desert

The time series of surface meteorological elements observed in Zamyn-Uud on 22–23 May 2013 are indicated in Fig. 3.15. Figures 3.16 and 3.18 show the time-height cross sections of the lidar observation results and meteorological conditions obtained from the NCEP FNL data, respectively, for Zamyn-Uud during the same period as in Fig. 3.15. Figure 3.17 indicates the time-height cross section of the aerosol extinction coefficients derived from the lidar observation result and time series of the aerosol optical thickness (AOT) calculated from the aerosol extinction coefficients. Three characteristic regions were found and are denoted with the letters I–K. As with Sainshand, a dust layer (region I) was located over the cold air (region J) and probably mixed with a cloud (region K).

The dust layer over the cold air is shown by medium attenuated backscatter coefficients ($1.6–4.0 \times 10^{-3}$ /km/sr, light blue to green) up to a height of about 4 km until 17 LST on 23 May (region I in Fig. 3.16a). The top height increased from 1.4 km at 03 LST to 3.8 km at 15 LST on 23 May. The thickness ranged from 0.3 to 1.7 km. The AOT for the dust layer was between 0.1 and 0.27 (Fig. 3.17b). In the dust layer, the volume depolarization ratio was 0.2–0.3 (Fig. 3.16b), and the volume color ratio was 1.0–2.4 (Fig. 3.16c). As with Sainshand, the dust layer was located in the updraft region (region I in Fig. 3.18b).

The sea level pressure increased by 13.4 hPa from 17 LST on 22 May to 11 LST on 23 May (Fig. 3.15a). The temperature decreased from 32.5 °C at 17 LST on 22 May to 18.4 °C at 05 LST on 23 May (Fig. 3.15b). The wind direction changed from southwest to northwest between 02 and 05 LST on 23 May (Fig. 3.15d). These characteristics show that the cold front (Fig. 3.1) passed through between 02 and 05 LST on 23 May, and the cold air replaced the warm air (Fig. 3.2).

Judging from the potential temperature and wind conditions, the cold air is indicated by region J below the dotted line in Fig. 3.18a. The top height of the cold air was about 1.0 km at

08 LST and 1.3 km at 14 and 20 LST on 23 May. The potential temperature in the cold air was 297–306 K. The wind directions rotated from north in the cold air to west above the cold air. This counterclockwise rotation is consistent with the cold air advection. The attenuated backscatter coefficients were small ($<1.6 \times 10^{-3}$ /km/sr, blue) in the upper part of the cold air (region J in Fig. 3.16a).

Region K, which is indicated by medium to large attenuated backscatter coefficients ($>1.6 \times 10^{-3}$ /km/sr, red) over a height of 2.2 km between 1700 and 1930 LST on 23 May, shows a cloud (Fig. 3.16a). It seems that the cloud was mixed with the dust layer. In the cloud, the volume depolarization ratio was mostly greater than 0.3 (Fig. 3.16b), and the volume color ratio was more than 3.0 (Fig. 3.16c). As with Sainshand, it is likely that the dust particles worked as ice nuclei. The ice crystals of the cloud were larger than the dust particles based on their color ratios.
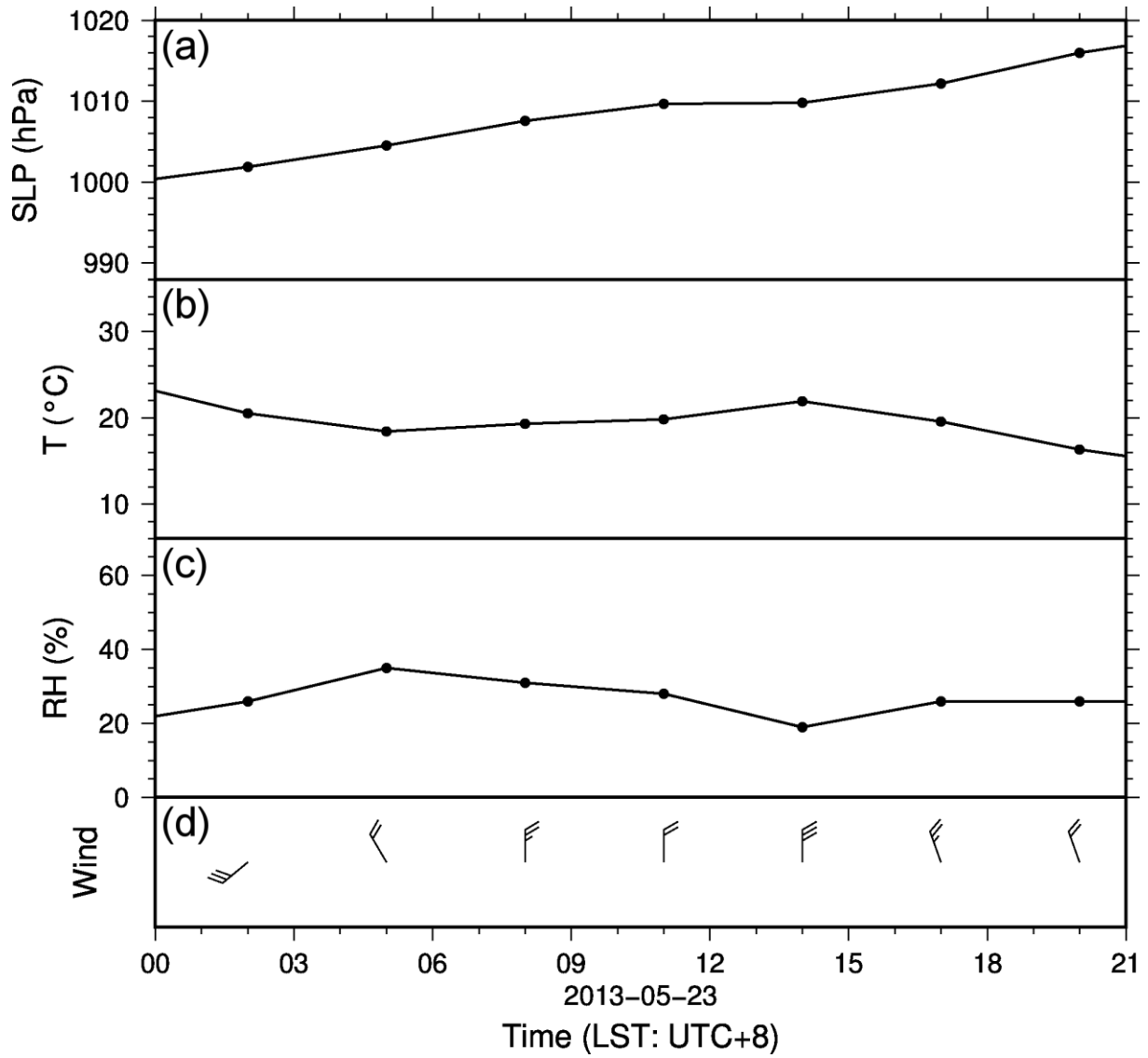
Figure 3.15: Same as Fig. 3.5, except that the location is Zamyn-Uud, and the period is from 00 to 21 LST on 23 May 2013.
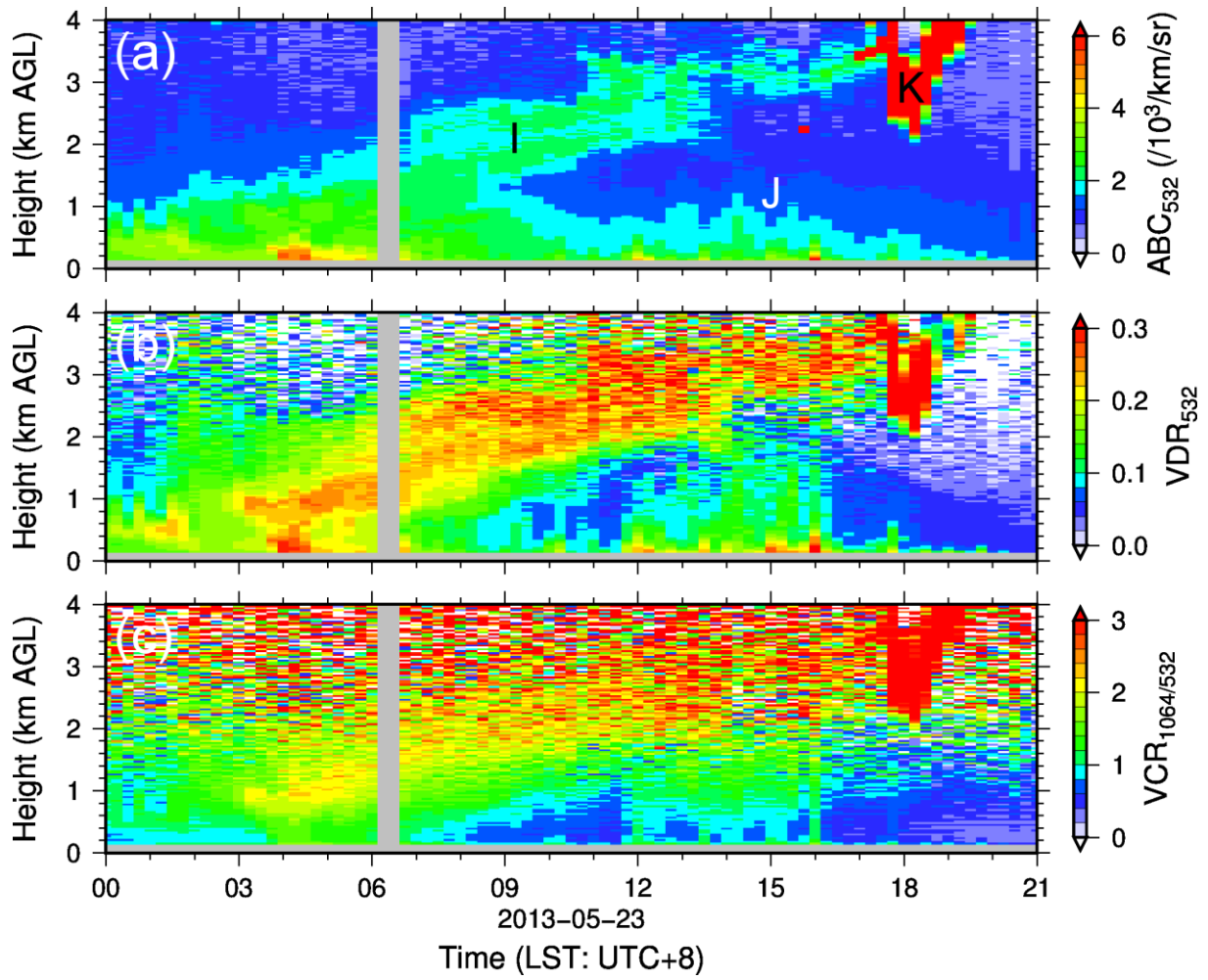
Figure 3.16: Same as Fig. 3.12, except that the location is Zamyn-Uud, the height range is 0–4 km, and the period is from 00 to 21 LST on 23 May 2013 (same as in Fig. 3.15). Regions I–K correspond to a dust layer, cold air, and a cloud, respectively.
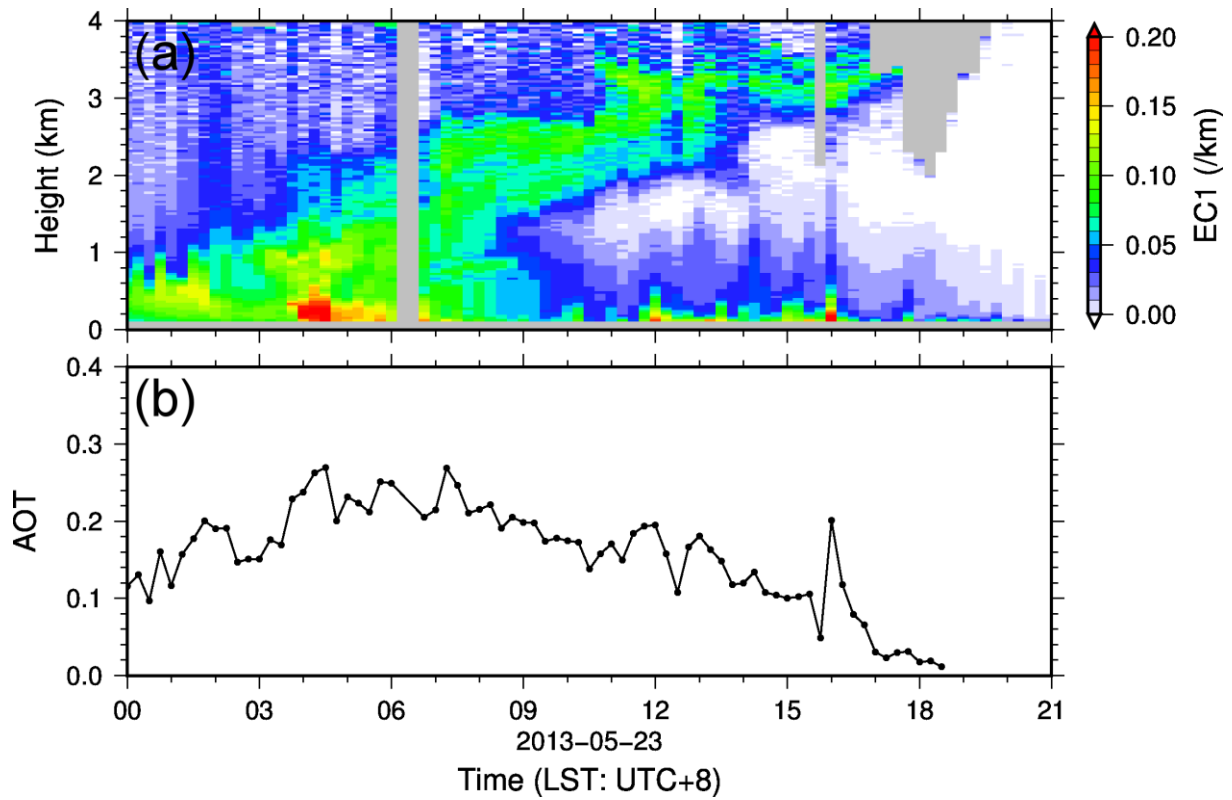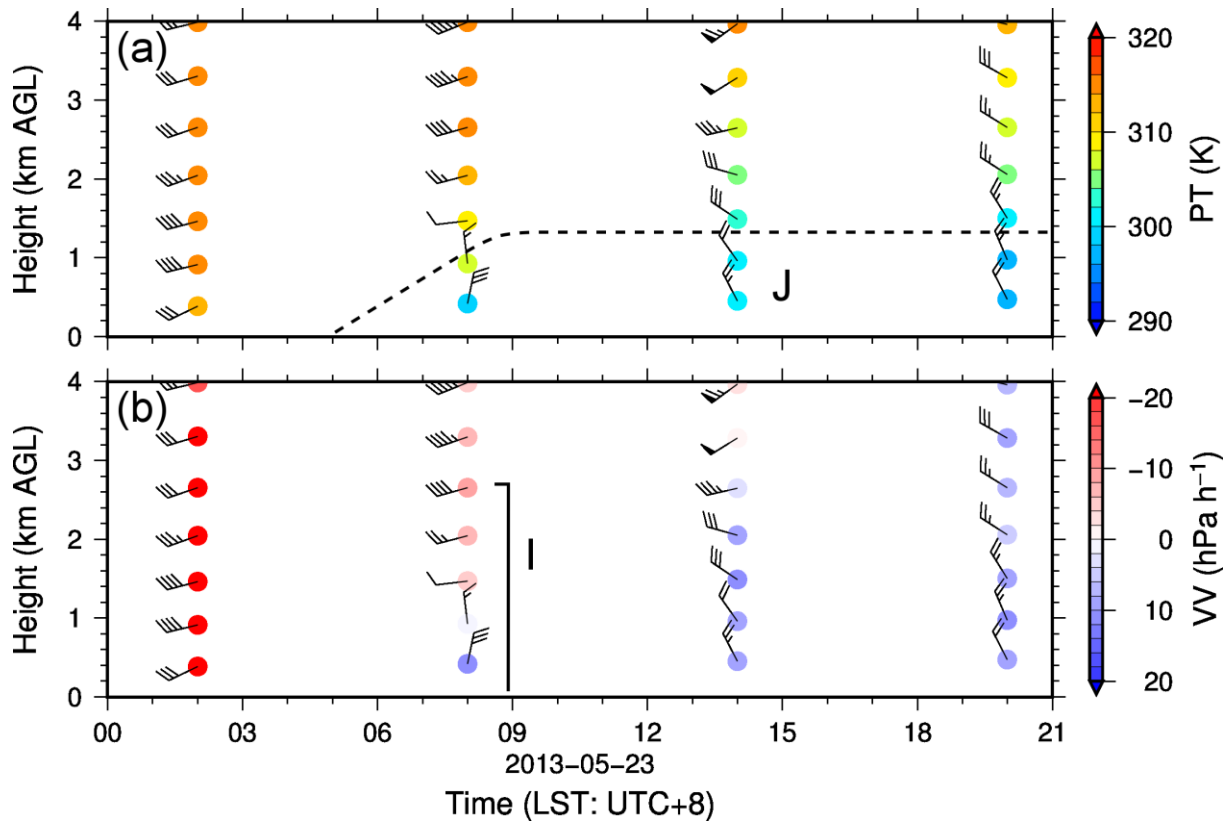
Figure 3.17: Same as Fig. 3.13, except that the location is Zamyn-Uud, and the period is from

00 to 21 LST on 23 May 2013 (same as in Fig. 3.15).

Figure 3.18: Same as Fig. 3.14, except that the location is Zamyn-Uud, and the period is from 00 to 21 LST on 23 May 2013 (same as Fig. 3.15). Regions I and J are the same as in Fig. 3.16.

4. Discussion

4.1 Vertical transport of dust by cold frontal system

In Dalanzadgad, a dust layer was distributed over the cold air along the cold frontal surface. In order to investigate the subsequent movement of the dust, the forward trajectories of the air parcels corresponding to the dust were analyzed and are indicated in Fig. 4.1. These trajectories show that the dust moved eastward to the eastern part of the Gobi Desert, particularly Zamyn-Uud (Fig. 4.1a). The dust ascended to a height of 2.0–2.7 km above ground level (AGL) for the first 13–15 hours, when it reached the eastern part of the desert (Fig. 4.1b). The relative humidity along the trajectories gradually increased from 40–50% to 70–80% while their height was increasing (Fig. 4.1c).

Figure 4.2 shows the observational model of the dust layer and the cold frontal system in Dalanzadgad on 22–23 May 2013. The distance from the position at 20 LST on 22 May, when the cold front passed, was calculated from the moving speed of the cold front (30 km/h), which is consistent with the wind speed (6–10 m/s). According to the moving direction of the cold front (southeast), the right and left sides indicate southeast and northwest, respectively.

In the general cold frontal system, warm air ascends along the cold frontal surface, which generates clouds (Wallace and Hobbs, 2006). In the present study, a cloud was observed at a height of 4 km AGL over the cold air near the cold front, which is the evidence of the ascending warm air. The lifted condensation level of the warm air estimated from the surface meteorological observation data was about 4 km AGL, which is consistent with the height of the cloud.

The reasons why the slightly large attenuated backscatter coefficients around a height range of 0.8–1.6 km AGL mentioned in Section 3.2 shows not cloud but dust are as follows: the attenuated backscatter coefficients were not so large compared with those of clouds; the height was lower than the lifted condensation level of the warm air. Therefore, it is concluded that the

52

ascending warm air in the cold frontal system transported the dust along the cold frontal surface from the dust storm in the atmospheric boundary layer to the free troposphere. The ascending warm air in a cold frontal system is one of the mechanisms that transport dust from the atmospheric boundary layer to the free troposphere, which can lead to the long-range transport of the dust by the middle-latitude westerlies.

The transport of dust from the atmospheric boundary layer to the free troposphere by the ascending warm air in a cold frontal system is also suggested by some previous studies. Alizadeh et al. (2012) simulated an Australian dust event in September 2009 by using a space-borne lidar (the Cloud-Aerosol Lidar with Orthogonal Polarization; CALIOP) and the WRF-Chem model. Hara et al. (2009) simulated Asian dust events in May 2007 by using the space-borne lidar CALIOP and a dust transport model. These studies showed the dust transport mentioned above based on numerical simulations. On the other hand, the present study shows the dust transport based on the continuous ceilometer observation in the source region of the dust.
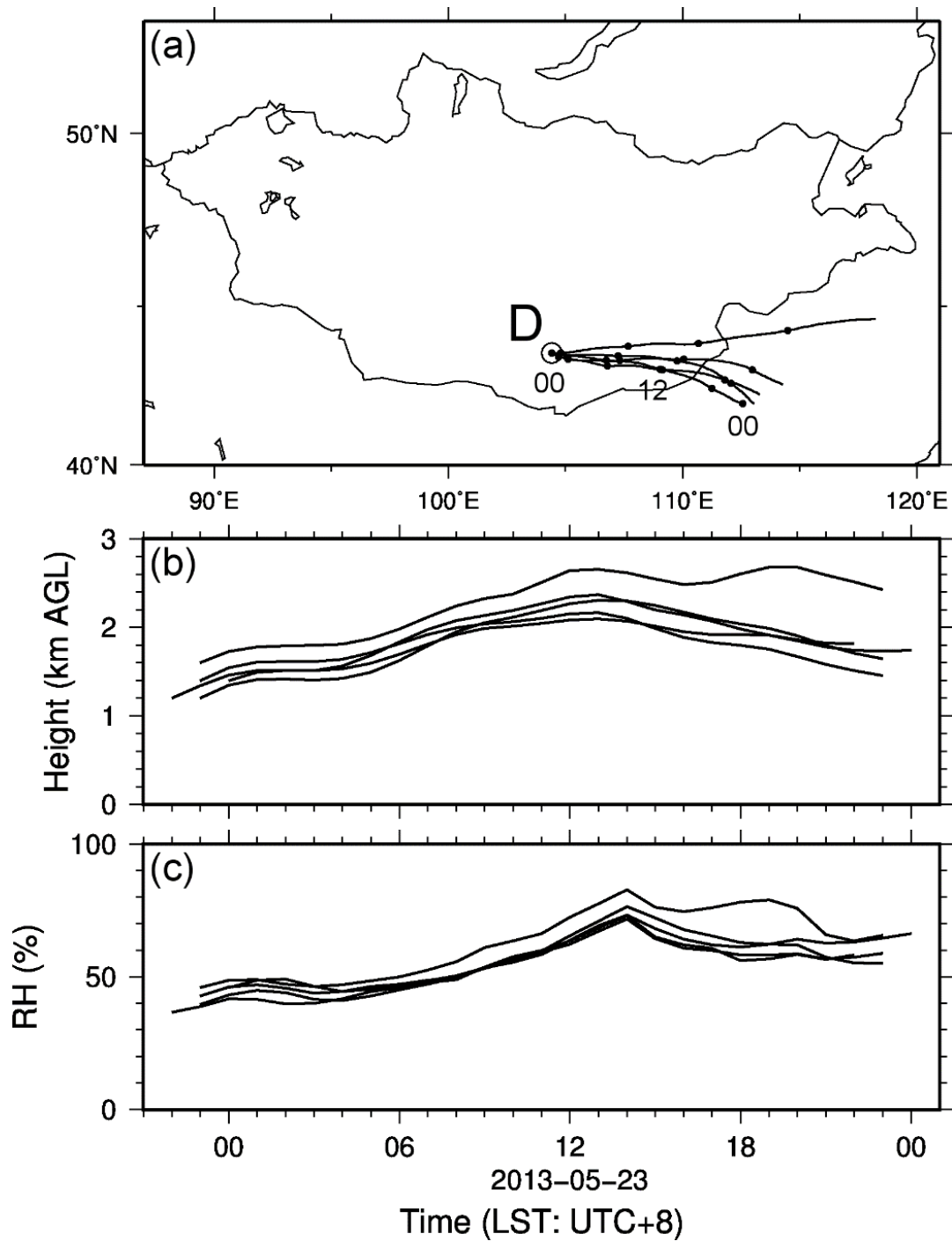
Figure 4.1: (a) The locations, (b) the height above ground level (AGL), and (c) the relative

humidity (RH) of 24-hour forward trajectories of air parcels corresponding to the dust that

was observed over the cold air in Dalanzadgad on 22–23 May 2013. In panel (a), the dots

on the trajectories indicate their location every 6 hours, and the numerical values of 00 and

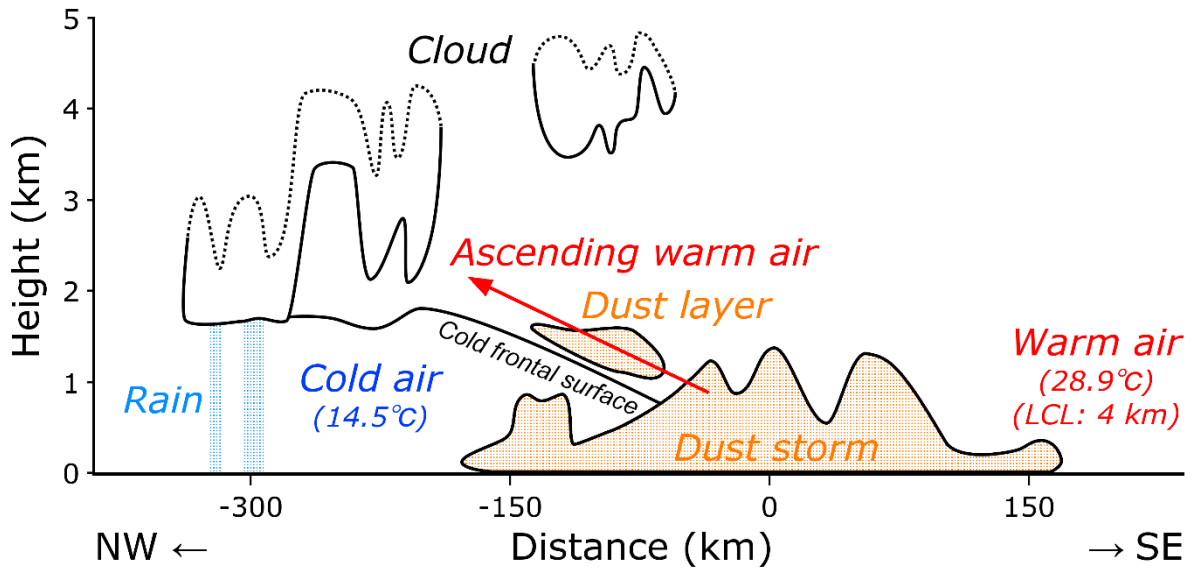12 near the trajectories represent the hours of 00 and 12 LST, respectively.

Figure 4.2: Observational model in Dalanzadgad on 22–23 May 2013. The distance of 0 km
indicates the leading edge of the cold air (i.e., the cold front on the ground). The distance
was calculated from the moving speed of the cold front (30 km/h). The right and left sides
indicate southeast (the moving direction of the cold front) and northwest, respectively.

4.2 Dust layer development caused by cold frontal system

Figure 4.3 illustrates the observational models at the lidar observation sites during the dust event. The characteristics of the dust layers over the cold air are summarized in Table 1. In Dalanzadgad, a dust storm occurred around the cold front and reached a top height of 1.6 km (Fig. 4.3a). A dust layer was located at a height of 0.9–1.6 km over the cold air, with a thickness that ranged from 0.2 to 0.5 km. In contrast, the dust layer observed in Sainshand and Zamyn-Uud reached a height of about 4 km (Figs. 4.3b and 4.3c) and were 1.6–2.5 and 0.3–1.7 km thick, respectively. Therefore, the dust layer produced during this dust event was developing upward from the atmospheric boundary layer (ABL) to the free troposphere while moving eastward through the Gobi Desert with the cold frontal system.

Figure 4.4 shows the estimated mechanism of the development of the dust layer during this dust event. It is suggested that this development was caused by the combination of the following two processes: (1) the continuous emission of dust from the desert surface to the ABL and (2) the continuous transport of the dust from the ABL up to the free troposphere.

Process (1): Dust was raised from the ground to the ABL over the Gobi Desert by the strong wind around the cold front. It is likely that the dust layer was supplied continuously with new dust from the desert surface while moving through the desert.

Process (2): The dust in the ABL was transported to the free troposphere by the updraft of the warm air in the cold frontal system. The updraft is shown in Figs. 3.14b, 3.18b, and 4.1b. This transport must have continued while the dust layer was moving through the desert with the cold frontal system.

Figure 4.5 illustrates the difference in the shapes of formed dust layers on different land surface condition. The dust layer observed in the Gobi Desert during this dust event was continuously distributed from the ABL to the free troposphere (Fig. 4.5a). This shape proves that the dust layer resulted from the continuous combination of the two processes mentioned

above. The present study establishes the mechanism of the dust layer development within the source region. In contrast, previous studies which observed dust layers in downwind regions show that the dust layers floated only in the free troposphere (Fig. 4.5b). When a dust layer moves from a desert to a non-desert region such as grassland, the emission of dust from the ground surface to the ABL (Process 1) finishes. The updraft of the warm air in a cold frontal system continuously transports the dust layer toward the free troposphere (Process 2). Then, the dust layer is distributed only in the free troposphere independently.

In conclusion, the cold frontal system induced the dust layer development from the ABL to the free troposphere in the Gobi Desert by the continuous combination of the two processes. This mechanism should have contributed to the long-range transport of the dust by the middle-latitude westerlies. It will be discussed below (Section 4.3) by using trajectory analyses.
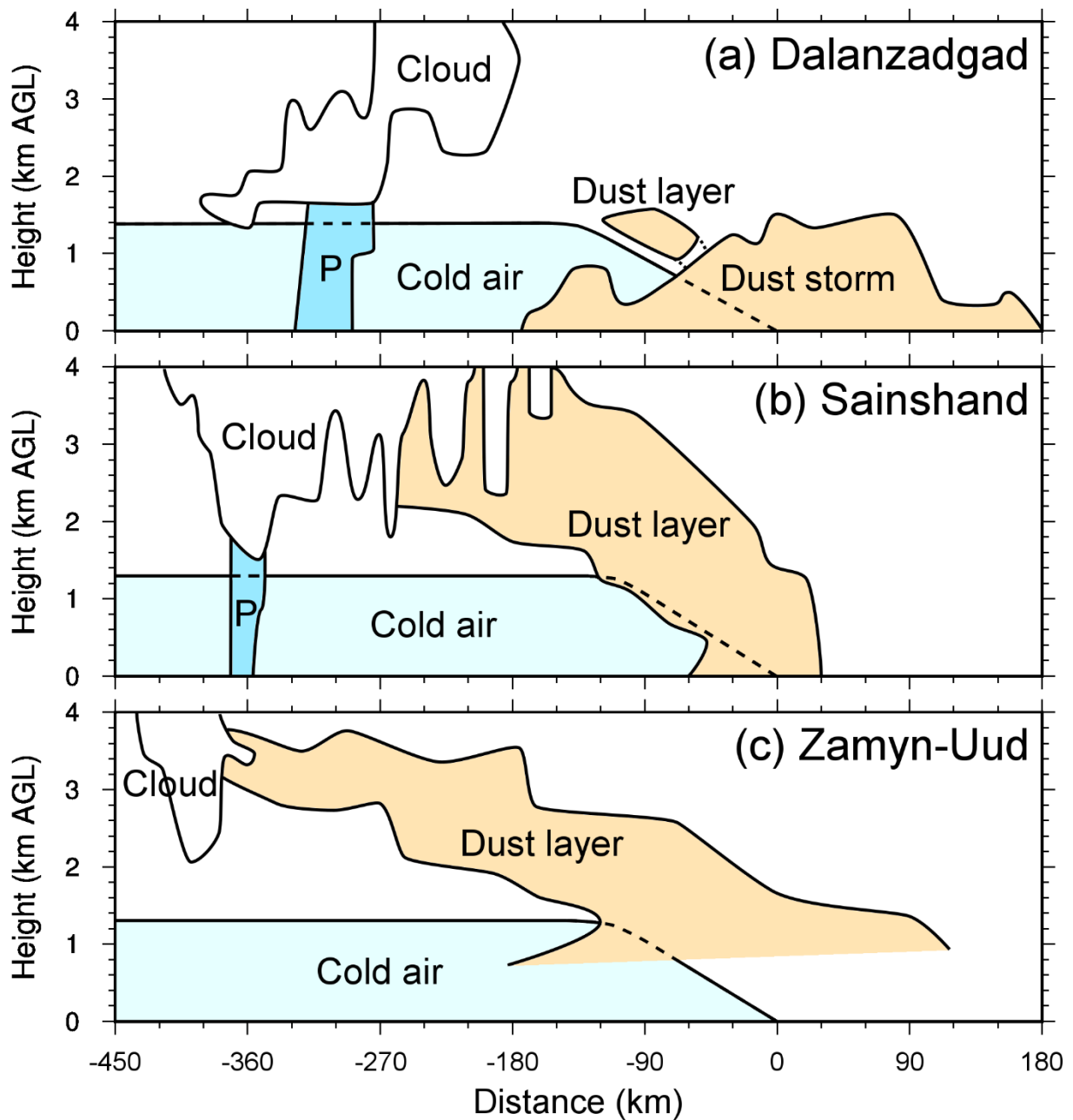
Figure 4.3: Observational models for (a) Dalanzadgad, (b) Sainshand, and (c) Zamyn-Uud at a height of 0–4 km during the dust event. The distance was calculated by using the moving speed of the cold front (30 km/h). The distance of 0 km indicates the leading edge of the cold air (i.e., the cold front on the ground) at each observation site. The right side is the moving direction of the cold front (southeast). The letter P denotes precipitation.

58

Table 1: Summary of the maximum top height and thickness range of the dust layer over cold

air observed in each site on 22–23 May 2013. In Sainshand, the presence of the dust layer

above a height of 4.0 km was unclear because of clouds.

Dust layer	Dalanzadgad	Sainshand	Zamyn-Uud
Maximum top height	1.6 km	(4.0 km)	3.8 km
Minimum thickness	0.2 km	1.6 km	0.3 km
Maximum thickness	0.5 km	2.5 km	1.7 km
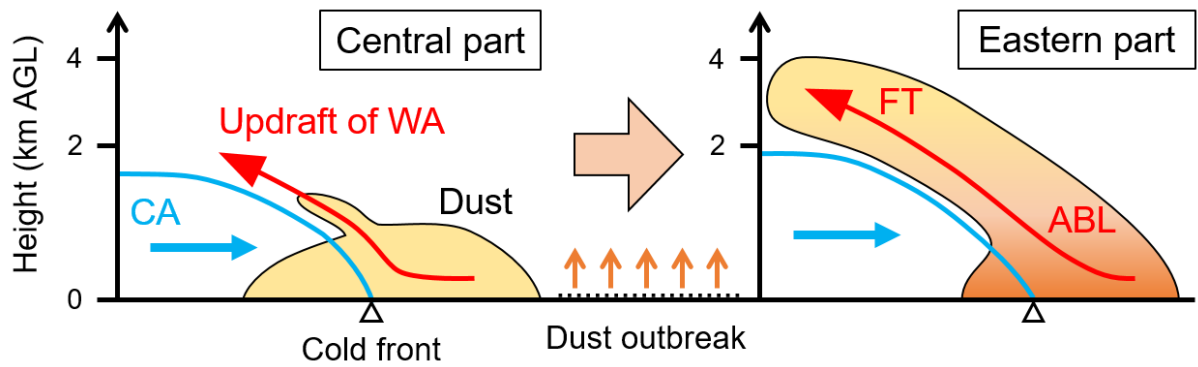
Figure 4.4: Observational model of the dust layer development caused by the cold frontal system in the Gobi Desert during the dust event. The left and right panels show the dust layer distributions in the central and eastern parts of the Gobi Desert, respectively. CA and WA denote cold air and warm air, respectively. While the cold front was moving through the Gobi Desert (from the central to the eastern part), dust was emitted from the ground surface to the atmospheric boundary layer (ABL) by the strong wind associated with the cold frontal system. The dust in the ABL was then transported to the free troposphere (FT) by the updraft of the warm air in the cold frontal system. These two processes occurred simultaneously and continuously and extended the dust layer from the ABL to the FT.
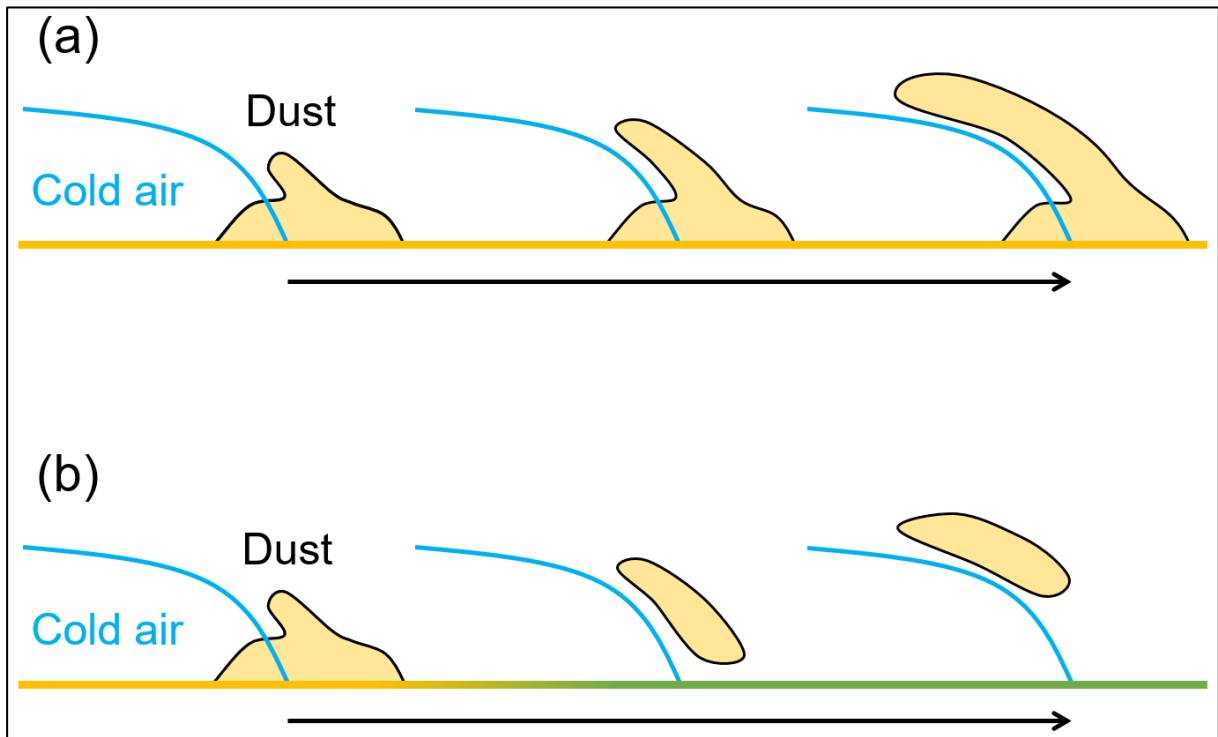
Figure 4.5: Difference in the shapes of formed dust layers on different land surface condition, i.e., (a) desert and (b) desert to grassland. The yellow and green colors of the lines indicate the land surface condition of desert and grassland, respectively. It is assumed that dust can be emitted from desert but not on grassland.

4.3 Long-range transport of dust

In Sainshand and Zamyn-Uud, a dust layer was observed from the atmospheric boundary layer to the free troposphere along the cold frontal surface. In order to investigate the subsequent movement of the dust, the forward trajectories of the air parcels corresponding to the dust were analyzed and are indicated in Figs. 4.6 (for Sainshand) and 4.7 (for Zamyn-Uud).

These trajectories show that the dust moved northeastward or eastward and reached northeastern China and Russian Far East (Figs. 4.6a and 4.7a). These moving directions are consistent with the westerlies above the cold air (Figs. 3.14a and 3.18a) and also the movement of the extratropical cyclone (Fig. 3.1).

Most of the dust ascended to a height of more than 4 km AGL, which corresponds to the free troposphere (Figs. 4.6b and 4.7b). This height increase must have been caused by the ascending warm air in the cold frontal system. It is possible that the dust was transported over a long range by the westerlies, as reported in previous studies (e.g., Kai et al., 1988; Husar et al., 2001; Hara et al., 2009; Yumimoto et al., 2009; Uno et al., 2009) (see Section 1.2).

The relative humidity along most of the trajectories exceeded 80% at a height of more than about 3 km (Figs. 4.6c and 4.7c). This high relative humidity shows the presence of clouds. The clouds should have been induced by the ascending warm air in the cold frontal system. It is suggested that the dust was mixed with the clouds in the free troposphere. The dust may have worked as ice nuclei, as suggested by Sakai et al. (2003) (see Section 3.3).
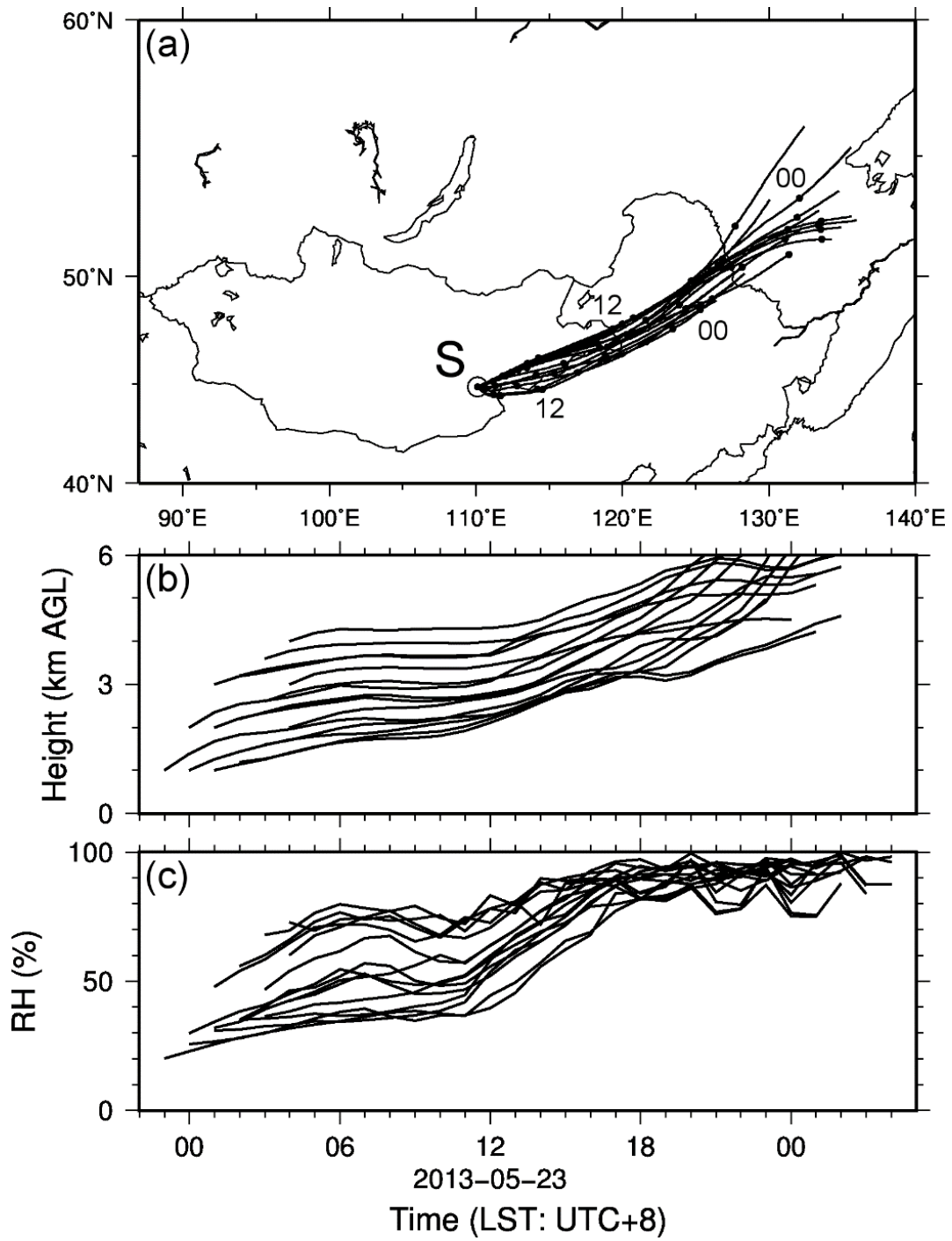
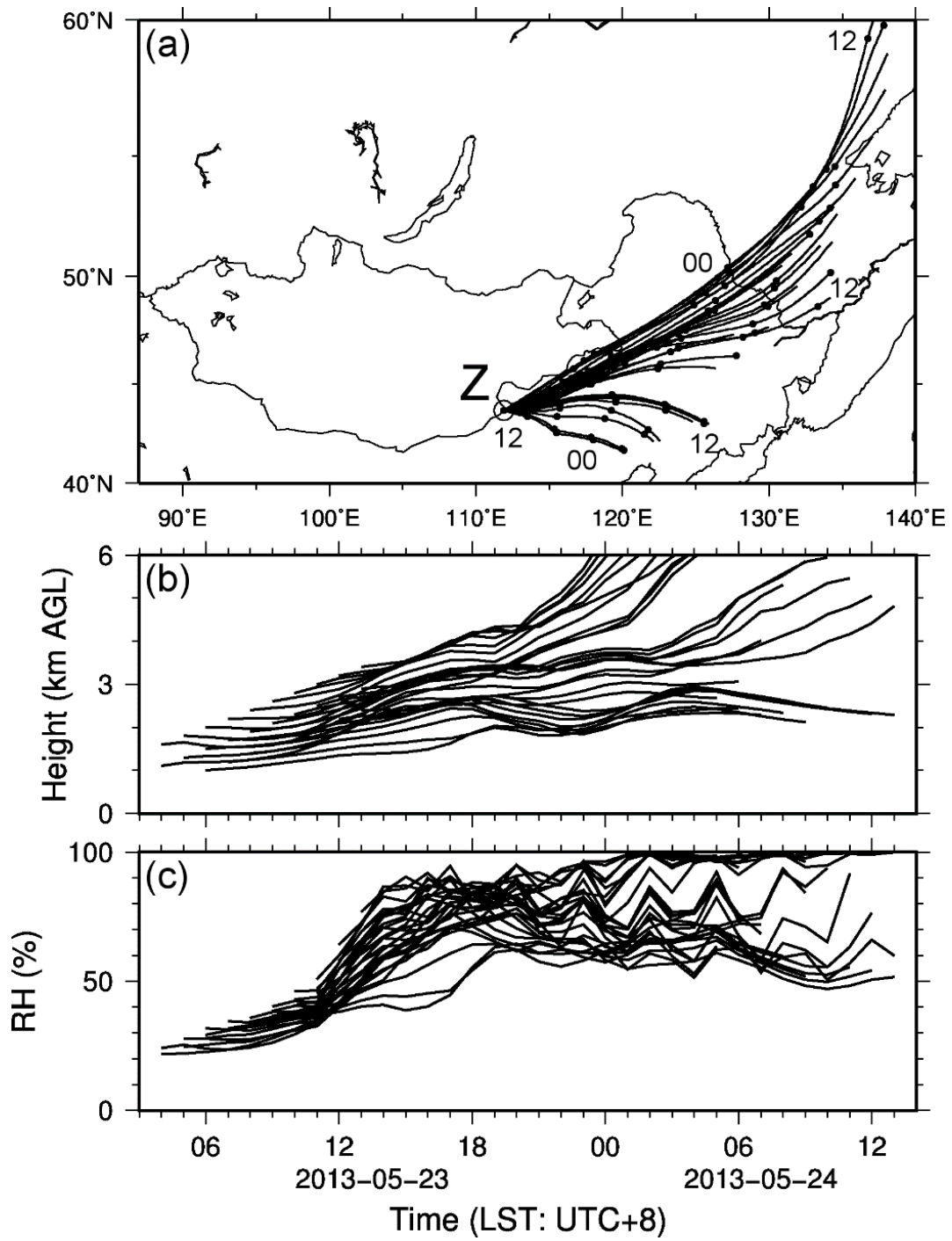Figure 4.6: Same as Fig. 4.3, except that the location is Sainshand.

Figure 4.7: Same as Fig. 4.3, except that the location is Zamyn-Uud, and the initial time of the forward trajectories is 23 May 2013.

5. Conclusion

A dust event occurred in the Gobi Desert on 22–23 May 2013 in association with the passage of a cold front. The spatial distribution of dust during the dust event was analyzed by using the Gobi Desert lidar network, which consists of a ceilometer in the central part of the desert (Dalanzadgad, Mongolia) and two AD-Net lidars in the eastern part of the desert (Sainshand and Zamyn-Uud, Mongolia). By combining the lidar network observation data with various meteorological data (e.g., the SYNOP data, NCEP FNL data, and NOAA HYSPLIT model), this study shows the spatial development of a dust layer by the cold frontal system and the subsequent long-range transport of the dust. The main findings of this study are summarized below.

(1) During this dust event, an extratropical cyclone moved northeastward from central Mongolia and developed with a cold front. The cold front crossed the Gobi Desert southeastward and sequentially passed through Dalanzadgad, Sainshand, and Zamyn-Uud. The cold front induced strong northerly winds (8–16 m/s) in the desert and emitted dust from the ground surface. Along the cold front, the cold air behind the cold front lifted up the warm air in front of the cold front.

(2) In Dalanzadgad (the central part of the Gobi Desert), a dust storm was generated by the strong wind (6–10 m/s) associated with the cold front. A part of the dust ascended along the cold frontal surface and reached a height of 1.6 km above ground level (AGL). It is suggested that the dust was transported from the dust storm by the ascending warm air in the cold frontal system. Then, the dust moved to the eastern part of the Gobi Desert together with the cold frontal system.

(3) In Sainshand and Zamyn-Uud (the eastern part of the Gobi Desert), a dust layer extended from the atmospheric boundary layer to the free troposphere along the cold frontal surface. The dust layer reached a height of about 4 km AGL and was mixed with cloud. The

distribution region of the dust layer corresponded to that of the ascending warm air in the cold frontal system.

(4) These results show that the dust layer was developing from the atmospheric boundary layer to the free troposphere while moving across the Gobi Desert with the cold frontal system. The mechanism of this development can be explained by two processes as follows: (a) the continuous emission of dust from the desert surface to the atmospheric boundary layer by the strong wind associated with the cold front and (b) the continuous transport of the dust from the atmospheric boundary layer to the free troposphere by the updraft of the warm air in the cold frontal system. This mechanism can lead to the long-range transport of dust by the westerlies in the free troposphere. It is the primary outcome of this study to capture the mass transport of a cold frontal system.

This study focused on the cold frontal activity which frequently induces dust outbreaks in the Gobi Desert, and showed the spatial structure of the generation and development of a dust layer caused by a cold frontal system. This outcome can contribute to the elucidation of the long-range transport of Asian dust and an improvement in the accuracy of climate models. In addition, it is important to maintain and expand the lidar network and analyze many dust events by using the observation data. This effort will help us better understand the mechanisms of the emission and transport of Asian dust.

constructive advice. I would like to appreciate all of them very much.

References

Adachi, S., and F. Kimura, 2007: A 36-year climatology of surface cyclogenesis in East Asia using high-resolution reanalysis data. *Sci. Online Lett. Atmos.*, **3**, 113–116.

Adachi, S., F. Kimura, S. Sugata, M. Hayasaki, Y. Kurosaki, and S. Wakamatsu, 2007: Dust transport along a cold front: A case study of a cyclone observed on 19-20 April 2000 in Northeast Asia. *J. Jpn. Soc. Atmos. Environ.*, **42**, 327–338.

Chen, S. -J., Y. -H. Kuo, P. -Z. Zhang, and Q. -F. Bai, 1991: Synoptic climatology of cyclogenesis over East Asia, 1958–1987. *Mon. Weather Rev.*, **119**, 1407–1418.

Duce, R. A., C. K. Unni, B. J. Ray, J. M. Prospero, and J. T. Merrill, 1980: Long-range atmospheric transport of soil dust from Asia to the tropical North Pacific: Temporal variability. *Science*, **209**, 1522–1524.

Hara, Y., K. Yumimoto, I. Uno, A. Shimizu, N. Sugimoto, Z. Liu, and D. M. Winker, 2009: Asian dust outflow in the PBL and free atmosphere retrieved by NASA CALIPSO and an assimilated dust transport model. *Atmos. Chem. Phys.*, **9**, 1227–1239.

Hayasaki, M., S. Sugata, and H. L. Tanaka, 2006: Interannual variation of cold frontal activity in spring in Mongolia. *J. Meteor. Soc. Japan*, **84**, 463–475.

Higashi, T., Y. Kambayashi, N. Ohkura, M. Fujimura, S. Nakanishi, T. Yoshizaki, K. Saijoh, K. Hayakawa, F. Kobayashi, Y. Michigami, Y. Hitomi, and H. Nakamura, 2014: Exacerbation of daily cough and allergic symptoms in adult patients with chronic cough by Asian dust: A hospital-based study in Kanazawa. *Atmos. Environ.*, **97**, 537–543.

Holben, B. N., D. Tanre, A. Smirnov, T. F. Eck, I. Slutsker, N. Abuhassan, W. W. Newcomb, J. Schafer, B. Chatenet, F. Lavenue, Y. J. Kaufman, J. V. Castle, A. Setzer, B. Markham, D. Clark, R. Frouin, R. Halthore, A. Karnieli, N. T. O'Neill, C. Pietras, R. T. Pinker, K. Voss, and G. Zibordi, 2001: An emerging ground-based aerosol climatology: Aerosol optical depth from AERONET. *J. Geophys. Res.*, **106**, 12067–12097.

Huang, J., T. Wang, W. Wang, Z. Li, and H. Yan, 2014: Climate effects of dust aerosols over East Asian arid and semiarid regions. *J. Geophys. Res.*, **119**, 11398–11416.

Huang, J., W. Zhang, J. Zuo, J. Bi, J. Shi, X. Wang, Z. Chang, Z. Huang, S. Yang, B. Zhang, G. Wang, G. Feng, J. Yuan, L. Zhang, H. Zuo, S. Wang, C. Fu, and J. Chou, 2008: An overview of the Semi-Arid Climate and Environment Research Observatory over the Loess Plateau. *Adv. Atmos. Sci.*, **25**, 906–921.

Husar, R. B., D. M. Tratt, B. A. Schichtel, S. R. Falke, F. Li, D. Jaffe, S. Gassó, T. Gill, N. S. Laulainen, F. Lu, M. C. Reheis, Y. Chun, D. Westphal, B. N. Holben, C. Gueymard, I. McKendry, N. Kuring, G. C. Feldman, C. McClain, R. J. Frouin, J. Merrill, D. DuBois, F. Vignola, T. Murayama, S. Nickovic, W. E. Wilson, K. Sassen, N. Sugimoto, and W. C. Malm, 2001: Asian dust events of April 1998. *J. Geophys. Res.*, **106**, 18317–18330.

Iwasaka, Y., H. Minoura, and K. Nagaya, 1983: The transport and spacial scale of Asian dust-storm clouds: A case study of the dust-storm event of April 1979. *Tellus*, **35B**, 189–196.

Jin, Y., K. Kai, K. Kawai, T. Nagai, T. Sakai, A. Yamazaki, A. Uchiyama, D. Batdorj, N. Sugimoto, and T. Nishizawa, 2015: Ceilometer calibration for retrieval of aerosol optical properties. *J. Quant. Spectrosc. Radiat. Transfer*, **153**, 49−56.

Jugder, D., M. Shinoda, N. Sugimoto, I. Matsui, M. Nishikawa, S. U. Park, Y. S. Chun, and M. S. Park, 2011: Spatial and temporal variations of dust concentrations in the Gobi Desert of Mongolia. *Global Planet. Change*, **78**, 14–22.

Kai, K., Y. Nagata, N. Tsunematsu, T. Matsumura, H.-S. Kim, T. Matsumoto, S. Hu, H. Zhou, M. Abo, and T. Nagai, 2008: The structure of the dust layer over the Taklimakan Desert during the dust storm in April 2002 as observed using a depolarization lidar. *J. Meteor. Soc. Japan*, **86**, 1–16.

Kai, K., Y. Okada, O. Uchino, I. Tabata, H. Nakamura, T. Takasugi, and Y. Nikaidou, 1988: Lidar observation and numerical simulation of a Kosa (Asian Dust) over Tsukuba, Japan

during the Spring of 1986. *J. Meteor. Soc. Japan*, **66**, 457–472.

Kawai, K., K. Kai, Y. Jin, N. Sugimoto, and D. Batdorj, 2015: Dust event in the Gobi Desert on 22−23 May 2013: Transport of dust from the atmospheric boundary layer to the free troposphere by a cold front. *Sci. Online Lett. Atmos.*, **11**, 156−159.

Kawai, K., K. Kai, Y. Jin, N. Sugimoto, and D. Batdorj, 2018: Lidar network observation of dust layer development over the Gobi Desert in association with a cold frontal system on 22–23 May 2013. *J. Meteor. Soc. Japan*, in press.

Kurosaki, Y. and M. Mikami, 2005: Regional difference in the characteristic of dust event in East Asia: Relationship among dust outbreak, surface wind, and land surface condition. *J. Meteor. Soc. Japan*, **83A**, 1–18.

Kwon, H. -J., S. -H. Cho, Y. Chun, F. Lagarde, and G. Pershagen, 2002: Effects of the Asian dust events on daily mortality in Seoul, Korea. *Environ. Res.*, **90**, 1–5.

Natsagdorj, L., D. Jugder, and Y. S. Chung, 2003: Analysis of dust storms observed in Mongolia during 1937–1999. *Atmos. Environ.*, **37**, 1401–1411.

Sakai, T., T. Nagai, M. Nakazato, Y. Mano, and T. Matsumura, 2003: Ice clouds and Asian dust studied with lidar measurements of particle extinction-to-backscatter ratio, particle depolarization, and water-vapor mixing ratio over Tsukuba. *Appl. Opt.*, **42**, 7103–7116.

Sassen, K., 2006: Polarization in lidar. *Lidar: Range-resolved optical remote sensing of the atmosphere*. Weitkamp, C. (ed.), Springer, New York, 19–42.

Shao, Y. P., and J. J. Wang, 2003: A climatology of Northeast Asian dust events. *Meteorol. Z.*, **12**, 187–196.

Shaw, G. E., 1980: Transport of Asian desert aerosol to the Hawaiian Islands. *J. Appl. Meteor.*, **19**, 1254–1259.

Shimizu, A., N. Sugimoto, and I. Matsui, 2010: Detailed description of data processing system for lidar network in East Asia. *Reviewed and revised papers of 25th Intl. Laser-Radar*

Conf., 911–913.

Shimizu, A., N. Sugimoto, I. Matsui, K. Arao, I. Uno, T. Murayama, N. Kagawa, K. Aoki, A. Uchiyama, and A. Yamazaki, 2004: Continuous observations of Asian dust and other aerosols by polarization lidars in China and Japan during ACE-Asia. *J. Geophys. Res.*, **109**, D19S17, doi:10.1029/2002JD003253.

Simpson, J. E., 1997: *Gravity currents: In the environment and the laboratory (2nd edition).* Cambridge University Press, 244 pp.

Smith, A., N. Lott, and R. Vose, 2011: The Integrated Surface Database: Recent developments and partnerships. *Bull. Amer. Meteorol. Soc.*, **92**, 704–708.

Stein, A. F., R. R. Draxler, G. D. Rolph, B. J. B. Stunder, M. D. Cohen, and F. Ngan, 2015: NOAA's HYSPLIT atmospheric transport and dispersion modeling system. *Bull. Amer. Meteor. Soc.*, **96**, 2059–2077.

Sugimoto, N., I. Matsui, A. Shimizu, T. Nishizawa, Y. Hara, C. Xie, I. Uno, K. Yumimoto, Z. Wang, and S. C. Yoon, 2008: Lidar network observations of tropospheric aerosols. *Proc. SPIE*, **7153**, 71530A, doi:10.1117/12.806540.

Sun, J., M. Zhang, and T. Liu, 2001: Spatial and temporal characteristics of dust storms in China and its surrounding regions, 1960-1999: Relations to source area and climate. *J. Geophys. Res.*, **106**, 10325–10333.

Takemi, T., and N. Seino, 2005: Dust storms and cyclone tracks over the arid regions in east Asia in spring. *J. Geophys. Res.*, **110**, D18S11, doi:10.1029/2004JD004698.

Tsunematsu, N., T. Sato, F. Kimura, K. Kai, Y. Kurosaki, T. Nagai, H. Zhou, and M. Mikami, 2005: Extensive dust outbreaks following the morning inversion breakup in the Taklimakan Desert. *J. Geophys. Res.*, **110**, D21207, doi:10.1029/2005JD005994.

Uno, I., K. Eguchi, K. Yumimoto, T. Takemura, A. Shimizu, M. Uematsu, Z. Liu, Z. Wang, Y. Hara, and N. Sugimoto, 2009: Asian dust transported one full circuit around the globe. *Nat.*

Geosci., **2**, 557–560.

Wallace, J. M., and P. V. Hobbs, 2006: *Atmospheric Science: An Introductory Survey (2nd Edition)*. Academic Press, 504 pp.

Wandinger, U., 2006: Introduction to lidar. *Lidar: Range-resolved optical remote sensing of the atmosphere*. Weitkamp, C. (ed.), Springer, New York, 19–42.

Wang, X., P. Zhai, and C. Wang, 2009: Variations in extratropical cyclone activity in northern East Asia. *Adv. Atmos. Sci.*, **26**, 471–479.

Wiegner, M., F. Madonna, I. Binietoglou, R. Forkel, J. Gasteiger, A. Geiß, G. Pappalardo, K. Schäfer, and W. Thomas, 2014: What is the benefit of ceilometers for aerosol remote sensing? An answer from EARLINET. *Atmos. Meas. Tech.*, **7**, 1979–1997.

Hostetler, C. A., Z. Liu, J. Reagan, M. Vaughan, D. Winker, M. Osborn, W. H. Hunt, K. A. Powell, and C. Trepte, 2006: *CALIOP algorithm theoretical basis document: Calibration and level 1 data products (PC-SCI-201)*. NASA Langley Research Center, Hampton, 66 pp.

World Meteorological Organization, 2011: *Manual on codes, International codes, vol. I.1, Annex II to the WMO technical regulations, part A, Alphanumeric codes, 2011 edition*. WMO, Geneva, 439 pp.

Wu, J. and K. Kai, 2016: Characteristics of dust outbreaks and their relation to strong wind and land surface conditions in the Gobi Desert and Northern China, 1999-2013. *J. Arid Land Stud.*, **26**, 51–57.

Wu, J., Y. Kurosaki, M. Shinoda, and K. Kai, 2016: Regional characteristics of recent dust occurrence and its controlling factors in East Asia. *Sci. Online Lett. Atmos.*, **12**, 187–191.

Yumimoto, K., K. Eguchi, I. Uno, T. Takemura, Z. Liu, A. Shimizu, and N. Sugimoto, 2009: An elevated large-scale dust veil from the Taklimakan Desert: Intercontinental transport and three-dimensional structure as captured by CALIPSO and regional and global models.

Atmos. Chem. Phys., **9**, 8545–8558.